Attosecond absorption and reflection spectroscopy of solids

N. Di Palo,[1] G. Inzani,[1, a)] G. L. Dolso,[1] M. Talarico,[1] S. Bonetti,[1] and M. Lucchini[1, 2, b)]

[1)] *Department of Physics, Politecnico di Milano, Piazza Leonardo da Vinci, 20133 Milano, Italy*

[2)] *Institute for Photonics and Nanotechnologies, IFN-CNR, 20133 Milano, Italy*

Since their introduction, all-optical spectroscopy techniques based on attosecond radiation have gained the attention of the scientific community because of their energy and time resolution, combined with an easier experimental implementation with respect to other approaches based on charged particle detection. Nowadays, almost ten years after the first application to a solid sample, attosecond transient absorption and reflection spectroscopy (respectively, ATAS and ATRS) have established as powerful tools to investigate how electrons can be excited and accelerated in matter with short light pulses, a key requisite to establish ultrafast switches in quantum electronics and overcome the current rate of data processing and information encoding. In this work, we start with a historical overview of the first pioneering experiments, to then introduce the fundamentals of both techniques. We conclude by discussing the current challenges and the possible future developments that are expected to bring ATAS and ATRS beyond their state of the art.

I. INTRODUCTION

The capability to follow and control ultrafast electron dynamics in matter with light pulses is a long-sought goal, with important implications in many fields of technology and research[1]. In a semiconductor, for example, charge injection by few-femtosecond infrared (IR) pulses could be used to turn the material into a conductive state, realizing ultrafast switches in optoelectronic devices, a milestone that promises to increase the limiting speed of data processing and information encoding, opening a new realm of information technology[2]. For this reason, the interaction between short optical pulses and matter has gained the attention of a broad scientific community in recent years, which demonstrated the more diverse applications[3–8]. This major breakthrough can only stem from a comprehensive knowledge of light-driven charge excitation, a cornerstone for energy and information transfer and a key challenge of modern solid-state physics and photonics[9,10]. Indeed, despite the continuous effort, the physical processes initiated by light in realistic and technologically relevant systems are still unclear[11–13].

In this work, we will discuss how attosecond all-optical pump-probe techniques, namely attosecond transient absorption spectroscopy (ATAS) and attosecond transient reflection spectroscopy (ATRS), have quickly established as powerful tools to investigate the ultrafast dynamics initiated by light in matter. We note that there are other all-optical techniques capable of accessing electron dynamics in solids with sub-cycle resolution and whose description goes beyond the scope of the present work. Remarkable examples are high-order harmonic spectroscopy[14–18] and four-wave mixing[19], for which recent reviews can be found at Refs.[20–22].

In Sec. II, we start by describing the application to atomic gas targets, to then recall the first pioneering experiments that brought to the extension of these techniques to solids[23]. Particular attention is given to the investigation of early dynamics that unfold during the interaction with light. Sections III and IV present the principles of the techniques. The current challenges and possible future developments are discussed in Sec. V, while the last section contains the conclusions.

II. HISTORICAL OVERVIEW

With the discovery of the high-order harmonic generation (HHG) process, it became clear that the extreme-ultraviolet (XUV) radiation emitted during the interaction between an intense IR pulse and a nonlinear medium could be used to obtain attosecond pulses[24–26]. This important discovery set the basis for the birth of attosecond science, whose goal is to resolve the electron motion in matter on its natural time scale[27–29]. The low efficiency of the HHG process (typically of the order of 10^{-6}-10^{-7}) limits the intensity of standard attosecond light sources. For this reason, attosecond pulses are usually combined with a portion of the generating IR pulses in order to perform pump-probe experiments without compromising the time resolution. First outstanding results have been obtained with spectroscopic techniques based on the detection of charged particles. Typically, a few-fs IR pulse perturbs the system inducing ultrafast dynamics that are subsequently probed by ionizing the sample with attosecond radiation and collecting the energy/momentum distribution of the resulting photoelectrons (or charged fragments). Despite offering unique features, such as being momentum-resolved[30,31], giving access to the 3D momentum distribution in the target frame[32,33] and enabling the study of continuum states[34,35], the techniques based on charged particle de-

a) Present address: Department of Physics, University of Regensburg, 93053 Regensburg, Germany
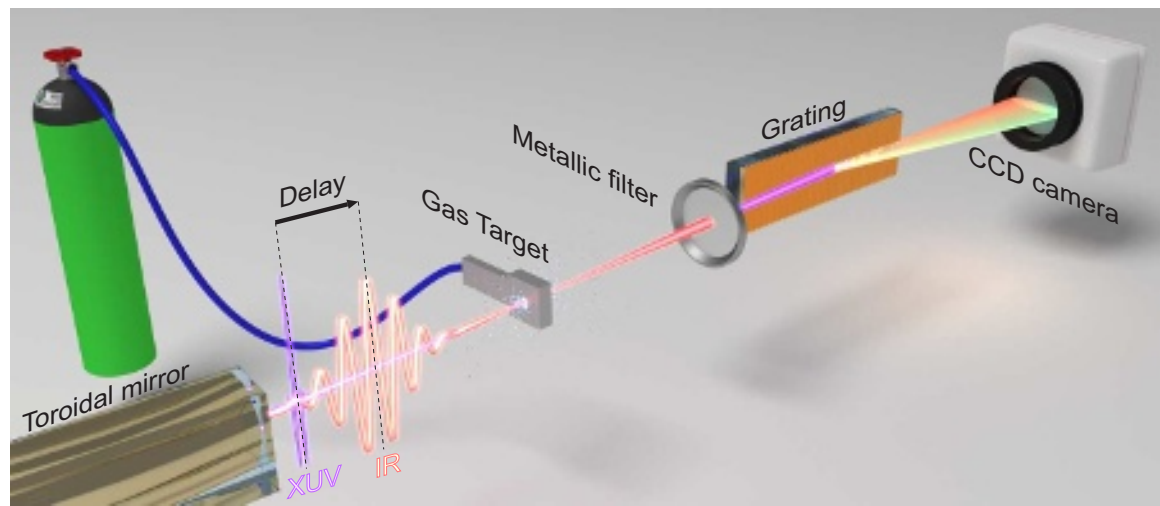
b) matteo.lucchini@polimi.it

FIG. 1. Cartoon of a typical ATAS setup for gas targets. After HHG, the few-fs IR pump pulse and the XUV attosecond probe are focused (in this case by a toroidal mirror) into a cell containing the gas target. After removing the pump radiation, typically with a metallic filter, the spectral content of the attosecond probe is recorded by an XUV spectrometer composed, in its simplest realization, by a dispersive grating and a CCD camera.

tection present some drawbacks. Space charge effects limit the maximum count rate per laser pulse, rendering the full exploitation of these techniques with the most common 1-kHz laser systems a formidable task. In addition, the relatively strong IR pump field (peak intensities of the order of 10^{10}-10^{12} W/cm^2) can generate a background via above-threshold ionization, which can be hard to remove. Being based on photon detection, all-optical techniques overcome these limitations and offer a complementary perspective on attosecond dynamics with the advantage of a generally easier experimental implementation.

A. Application to gas targets

Transient absorption spectroscopy (TAS) is nowadays a well-established approach to study ultrafast dynamics in a variety of samples and temporal regimes[36,37]. In brief, a pump pulse initiates the dynamics which is then followed by monitoring the spectral content of a probe pulse transmitted through the target (Fig. 1). The first application of XUV radiation generated via HHG to TAS was reported in 2007[38,39] when Loh and coworkers investigated the strong-field ionization of Xe atoms by an intense 800-nm pulse. A few years later, three groups demonstrated independently the possibility to use such a scheme to obtain attosecond time resolution in TAS[40–42], showing its potential in probing the behavior of bound states, not always directly accessible with conventional attosecond spectroscopy techniques[43].

These first inspiring experiments started a new branch in attosecond science, which considerably increased our understanding of fundamental light-matter interactions in rare gas atoms[36]. A variety of relatively recent publications have addressed absorption of XUV radiation in noble gases either by using single attosecond pulses or attosecond pulse trains[44–49], shining light onto a multitude of different competing effects in photoionization like sub-cycle AC Stark shift, light-induced states, electron wave-packet interference, Fano resonances, Autler-Townes splitting, and quantum beating (Fig. 2). Additionally, ATAS provides a robust and precise way to perform time-delay calibration in pump-probe experiments[50].

The employment of attosecond pulses in the XUV spectral region offers the unique possibility to simultaneously probe optical transitions that involve diverse core levels, rendering the spectroscopic technique element-specific and sensitive to coordination chemistry and oxidation state. These aspects are particularly important when dealing with more complex targets like molecules and solids, characterized by a congested photoelectron spectrum which hinders the correct application of most of the standard techniques based on charged-particle detection. ATAS has thus become one of the most powerful tools for the study of ultrafast dynamics in molecules. The first application to a molecular target traces back to 2016 when ATAS was applied to study vibrational and autoionization dynamics in H_2[51] and N_2[52,53]. Since then, ATAS has been used to investigate a plethora of fundamental physical processes, like conical intersection in diatomic[54] and poliatomic molecules[55–57], and charge migration in SiH_4[58]. Fostered by the development of novel laser sources and HHG schemes capable of producing energetic XUV photons in a tabletop setup, this spectroscopic technique has more recently been extended to the water window[59–62], all-XUV schemes[63] and liquid targets[64], further proving its versatility and capability to
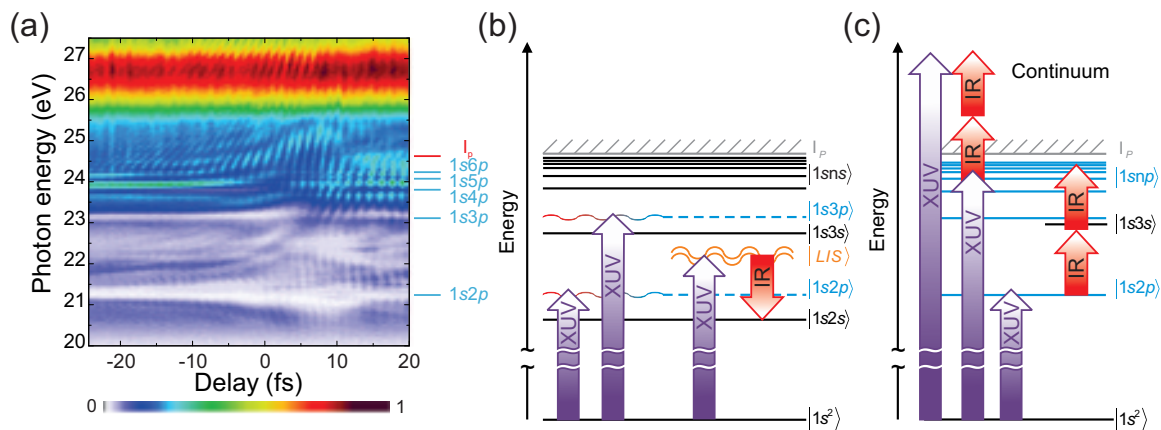
FIG. 2. **(a)** Spectral intensity of a single attosecond pulse transmitted through a dense He target pumped by a delayed IR few-fs pulse. The light blue lines on the right identify the atomic states accessible by single-photon XUV excitation, while I_p indicates the ionization potential. The trace presents clear fast modulations and distortions of the atomic lines which can be explained in terms of optical Stark shift and light-induced states (LIS), **(b)**, as well as "which-way" interference between direct and IR-assisted XUV excitation, **(c)**. Reproduced from[47]. ©IOP Publishing and Deutsche Physikalische Gesellschaft. CC BY 3.0.

disclose ultrafast dynamics in complex systems.

B.   Extension to solid samples

Despite transient absorption schemes being more diffused, probably because of the easier experimental setup and theoretical interpretation (see Sec. III), the first example of all-optical spectroscopy in solids with harmonic radiation employed a reflection geometry[65]. In their work, Papalazarou and co-workers studied coherent phonon dynamics in a Bi(111) single crystal by collecting the reflected harmonic radiation with an XUV photodiode (Fig. 3(a)). The energy-integrated sample reflectivity (Fig. 3(b)) showed clear oscillations associated with the A_{1g} phonon mode. R. Géneaux and co-workers have recently revisited this experiment, using a single attosecond pulse (Fig. 3(c)) and resolving in energy the spectra of the reflected radiation[66]. The resulting transient reflectivity trace (Fig. 3(d)) shows a rich oscillating signal that can be decomposed into the contribution of phonon motion (edge shift), holes photoexcited in the valence band (VB), and electrons in the conduction band (CB), thus obtaining a direct view into the energy balance of this Peierls-distorted system.

Reflectivity schemes have also been relatively early combined with dispersive targets to study femtosecond and picosecond magnetism in a HHG-based setup[67,68]. Nevertheless, the first experimental extension to the attosecond realm has been obtained in absorption geometry by Schultze and coworkers, who used a 4-fs IR pulse to pump a 125-nm thick SiO_2 sample and probed its response with a 72-as pulse centred around $105\,eV$[69]. By collecting the XUV transmitted spectra as a function of the pump-probe delay the authors could retrieve

the transient absorbance of the material (see Sec. III), which showed a clear signal around $\sim 99\,eV$, corresponding to the $L_{2,3}$ edge of silicon. This signal lasts only during the pump-probe temporal overlap and exhibits a modulation that oscillates with twice the pump pulse central frequency, ω, (see Fig. 4). This pioneering result not only proved that a short and intense IR pulse could be used to induce a reversible polarization, effectively turning an insulator into a conductive state on unprecedented time scales, but also demonstrated the capability of ATAS to investigate the elusive strong field phenomena which unfold during light-matter interaction (see Sec. II C). The chemical sensitivity, broad-band probing, and extreme time resolution, made ATAS a versatile tool, capable of disentangling ultrafast physical processes in a variety of solid samples[29,37,70]. Remarkable examples are: charge transfer in metal oxides like $\alpha-Fe_2O_3$[71] and Co_3O_4[72], electron, holes and lattice dynamics in semiconductors[73–75], metal-to-insulator transitions (MIT) in vanadium dioxide[76], formation of coherent optical phonons[77] and polarons[78], core exciton dynamics[79] (Figs. 6(a) and 6(b)), ultrafast screening and localization dynamics in semiconductors[80] and metals[81,82], as well as optically-induced spin and momentum transfer in a magnetic system[5].

Despite relaxing some big constraints related to the sample preparation and heat dissipation (see Sec. IV), HHG-based transient reflectivity experiments took longer to be extended to the attosecond domain. In 2018, Kaplan and coworkers investigated electron and hole dynamics in Ge, pumping the sample with 5-fs IR pulses and probing its reflectivity with an attosecond pulse centred around $M_{4,5}$ Ge edge ($\sim 29.5\,eV$, Fig. 5(a))[83]. By exploiting the enhanced sensitivity at the critical angle for total external reflection[84] (see Sec. IV), and fitting
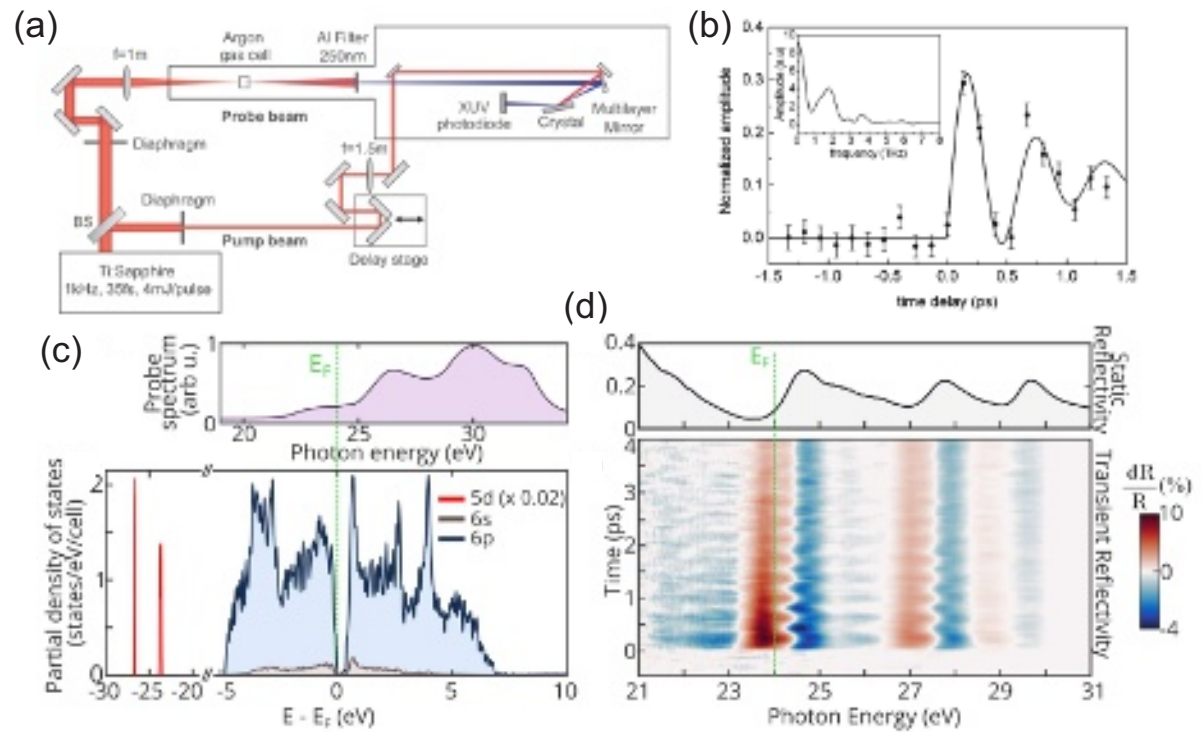
FIG. 3. **(a)** A schematic representation of the pump-probe experimental setup used in Ref.[65]. **(b)** Measured normalized Bi reflectivity showing the oscillations related to the coherent phonon initiated by the IR pulse. The inset shows its Fourier transform. **(c)** XUV probe spectrum (top panel) used in Ref.[66] and partial density of states per atom computed with density functional theory (DFT, bottom panel). **(d)** Measured energy-resolved static reflectivity of Bi (top panel) and its IR-induced relative changes obtained by scanning the delay between the pulses over 4 ps. The green dashed line indicates the Fermi level.Panels (a) and (b) reproduced from[65], with the permission of AIP Publishing. Panels (c) and (d) are reproduced from[66]. CC BY 4.0.

the transient reflectivity trace with an analytical model, the authors could retrieve the contribution of electrons, holes and band shifting, accessing carrier and phonon thermalization kinetics on a time scale that ranges from hundreds of fs to few ps (Fig. 5).

Using a similar scheme, Géneaux and collaborators employed ATRS to study ultrafast core-exciton dynamics in MgO[85] (Figs. 6(c) and 6(d)). Starting from the measured reflectivity, the authors retrieved the sample absorption through Kramers-Kronig (KK) relations[86], and studied the physical processes responsible for the ultrafast decay of the excitonic quasi-particle formed by an Mg $2p$ hole and an electron in the material CB. The results show that these particles have a lifetime of the order of 2 fs, dictated by Auger decay and coupling with phonons (the latter being the dominant).

One year later, Lucchini and coworkers studied a similar ionic insulator, MgF_2, realizing the first ATRS experiment to report sub-cycle dynamics and thus extending the technique to the attosecond domain[87] (Figs. 6(e) and 6(f)). Similarly to the experiment in MgO, the authors measured the reflectivity of a magnesium fluoride single-crystal around the Mg $L_{2,3}$ edge and observed a clear signature of an excitonic state at 54.4 eV (marked with

A and A' in Fig. 6(e)). The few-femtosecond component in the differential reflectivity trace (Fig. 6(e)) well compares to the previous results obtained in SiO_2 and MgO, and originates mainly from the optical Stark effect[88]. As such, it can be explained with a model where dark and bright excitons are described by non-dispersive (atomic-like) states[89], and from which it is possible to retrieve relevant information on the quasi-particle, such as its Auger decay rate or coupling with phonons[90]. The MgF_2 differential reflectivity further shows a faster component that oscillates with twice the IR pump frequency, ω. Theoretical calculations based on a 1D Wannier-Mott model could reproduce the measured reflectivity, including the fast component (Figs. 6(f) and 7(a)). At first sight, a pure atomic-like model (Fig. 7(b)) seems to fairly reproduce the total response, while a solid-like parabolic model fails (Fig. 7(c)), suggesting that also the sub-cycle excitonic response originates from the optical Stark effect. A closer inspection, made possible by an absolute calibration of the pump-probe delay axis[91], reveals instead the opposite scenario. The absolute phase delay of the 2ω oscillations in the experimental trace (black solid curve in Fig. 8) shows a V-shaped dispersion reproduced by the full model (red solid curve in Fig. 8). The crystal-
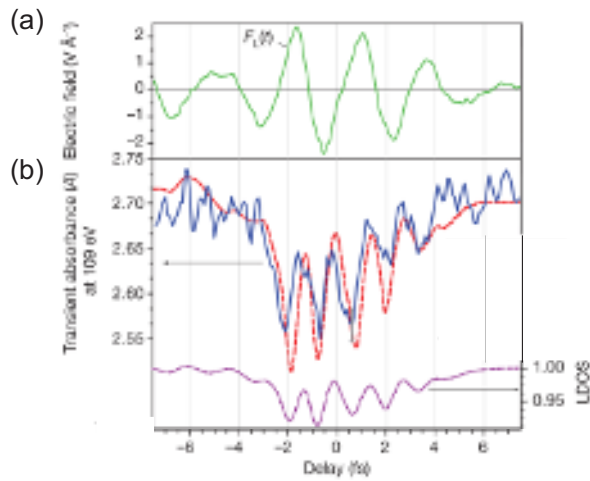
(a)

(b)

FIG. 4. **(a)** IR electric field used to pump the SiO_2 sample in Ref.[69]. **(b)** SiO_2 transient absorbance obtained by integrating the transmitted attosecond spectra in a 1-eV wide energy window centered at 109 eV (blue curve). The transient signal recovers soon after the temporal overlap and shows clear 2ω-oscillations correctly reproduced by the theoretical prediction (red dashed curve). The dashed violet curve on the bottom shows instead the calculated local density of states (LDOS) at the position of a Si atom. Reprinted by permission from Springer Nature Customer Service Centre GmbH: Nature[69]. Copyright (2013).

only contribution (gray dashed curve in Fig. 8) shows a similar V-shaped dispersion but centered around the bottom of the CB. This particular dispersion gives rise to a fish-bone structure in the experimental trace which is linked to the time-resolved dynamical Franz-Keldysh effect (DFKE)[92–94]. Calculations performed by considering only the atomic-like excitonic states (orange dotted curve in Fig. 8) fail in retrieving the correct phase delay, even qualitatively. This suggests that the dual nature (atomic and solid) of the excitonic quasi-particle unfolds on different time scales. On a few-fs time scale, the exciton dynamics can be fully explained with an atomic model as dictated by the optical Stark effect. On an attosecond time scale, instead, the transient optical response originates from intra-band motion in dispersive solid-like states. This example underlines how the extreme time resolution of ATRS can be exploited to disentangle effects previously found to compete in time-integrated measurements and open new perspectives on our knowledge of ultrafast carrier dynamics in solids.

C. Sub-cycle charge dynamics

With their extreme time resolution, ATAS and ATRS offer the unique possibility to disclose the complex and interlaced physical processes that unfold during the interaction with a light pulse[95–97]. This is particularly relevant in the strong-field regime where mechanisms like single- and multi-photon absorption (Fig. 9(a)), tunnel excitation (Fig. 9(b)), intra-band motion (Fig. 9(c)), band dressing and formation of Floquet states (Fig. 9(d)), are expected to compete in defining carrier injection[98]. In this complex regime, far from being completely understood[11,12], it is not always possible to easily determine, *a priori*, the exact weight and contribution of all the phenomena listed above.

Nevertheless, in certain cases, the dominant light-matter interaction regime can be predicted starting from well-known adiabaticity parameters. Remarkable examples are the Keldysh parameter, γ_K, and the adiabaticity parameter γ_a. The former has been derived by considering quasi-static fields with respect to the electron dynamics time scale (i.e., pump photon energies much smaller than the minimal direct band gap) and it is equal to $\gamma_K = \omega\sqrt{m^*\Delta}/(|e|E_0)$, where ω and E_0 are the field central frequency and amplitude inside the material, Δ and m^* are instead the material energy gap and reduced electron-hole mass, while e is the electron charge. γ_K is often used to discriminate between multiphoton absorption ($\gamma_K \gg 1$) and tunnel excitation ($\gamma_K \sim 1$), also in cases where the applicability of the Keldysh theory is not always clear. The adiabatic parameter γ_a is instead defined as the ratio between the field ponderomotive energy, U_p, and the photon energy: $\gamma_a = U_p/(\hbar\omega) = e^2E_0^2/(4m^*\hbar\omega^3)$. It helps in determining whether the field is better described by a classical ($\gamma_a \gg 1$) or quantum ($\gamma_a \ll 1$) picture. In between ($\gamma_a \sim 1$), the field description transits from classical to quantum, and its interaction with matter is dominated by exotic phenomena like the DFKE[99], often referred to as photon-assisted tunneling.

As it is easy to imagine, due to the complexity of the problem, it is not always possible to resort to a single parameter to frame the whole interaction regime. In 2021 Heide and co-workers proposed to intersect the prediction of several well-known parameters and studied a parabolic two-band model[100]. Making use of the Keldysh parameter γ_K, the multiphoton parameter $M = \Delta/(\hbar\omega)$, the resonant parameter $z_R = 2\Omega_R/\omega$ (where Ω_R is the Rabi frequency), and the Landau-Zener transition probability $P_{LZ} = \exp\{-2\pi\delta_{LZ}\}$ (with $\delta_{LZ} = \gamma_K\Delta/(4\hbar\omega)$ being the Landau-Zener adiabaticity parameter), they identified five distinct interaction regimes which are summarized in Fig. 10. For weak electric fields ($\gamma_K > 1$) light-matter interaction is well described by a *perturbative multiphoton absorption regime* (Fig. 10, panel ①). If the resonant condition is matched, i.e. if M is an integer (blue curves in the main panel of Fig. 10), the electron population in the CB, ρ_{CB}, gradually rises during the interaction, establishing a net residual population of excited real charges (black curve in Fig. 10①). The interaction at $M = 1$ is well described by Rabi oscillations, where the residual excited population depends on the pulse area. When the Keldysh parameter approaches unity, the effect of the strong field can no longer be neglected. Due
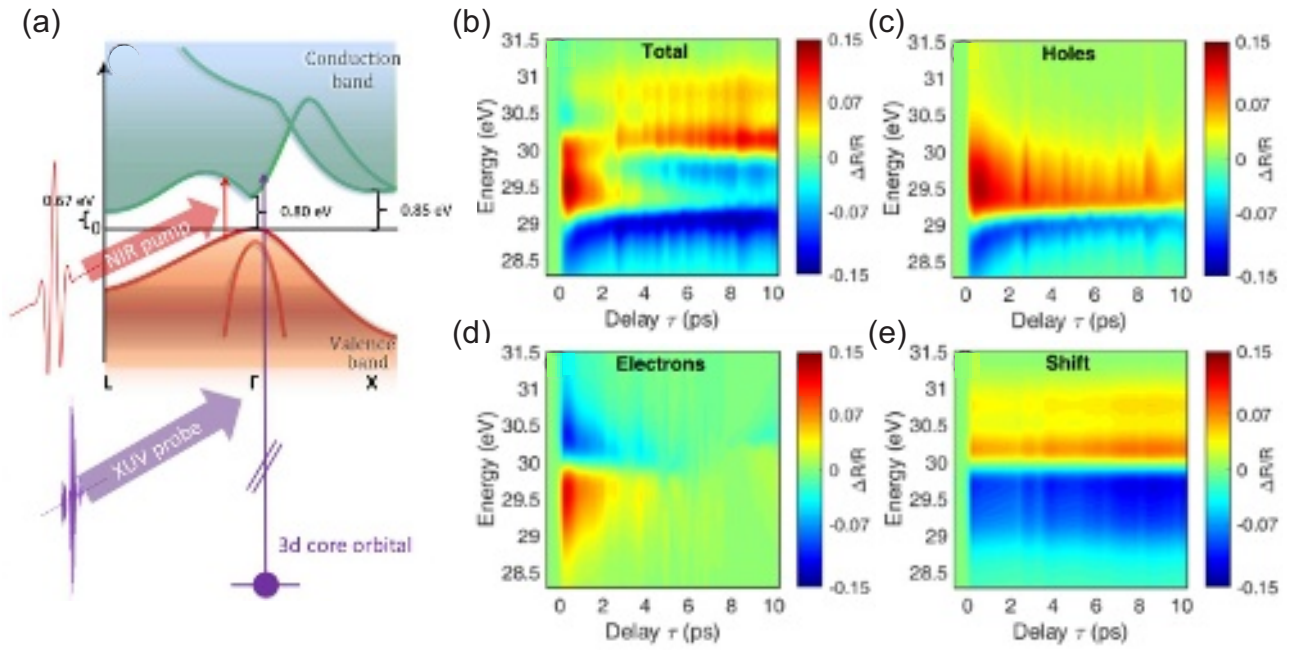
FIG. 5. **(a)** Schematic of the pumping mechanism used in[83] to study electron and hole dynamics in Ge. A few-fs IR pulse promotes electrons from the material VB to the CB, creating a non-equilibrium distribution whose subsequent fast relaxation is probed by a single attosecond pulse through a resonant transition at the Ge $M_{4,5}$ edge. The total transient reflectivity trace, **(b)**, is then decomposed in the contribution coming from holes, **(c)**, electrons, **(d)**, and rigid energy shift, **(e)**. Reprinted figure with permission from[83], Copyright (2018) by the American Physical Society.

to a strong AC Stark effect, for $\gamma_K \ll 1$, the resonance condition is no longer expressed by the blue curves and carrier-wave Rabi flopping can occur[101]. The portion of the diagram where $\gamma_K < 1$ can be divided in four different regions. If $z_R > 1$ and $P_{LZ} \simeq 1$ the interaction falls into an *impulsive Landau-Zener regime* (Fig. 10②) where the electrons are excited back and forth during an optical cycle, leaving no residual excitation after the interaction with the pulse. The same situation is found for the region where $z_R < 1$ and $P_{LZ} > 0.5$, which defines the *non-impulsive Landau-Zener regime* (marked with ③ in Fig. 10). Even if the transition probability is large, the transition time is longer than the optical cycle, resulting in a transient ρ_{CB} that recovers following the pulse envelope. If P_{LZ} is small, the interaction is instead in an *adiabatic regime*, where only intraband motion and excitation of virtual charges are observed (Fig. 10④). Finally, if $P_{LZ} \sim 0.5$, $M > 1$ and $\gamma_K \ll 1$, light-matter interaction is described by the *adiabatic-impulsive Landau-Zener-Stückelberg regime* (Fig. 10⑤), where the CB excitation probability is determined by Landau-Zener-Stückelberg interference between coherent transitions where part of the electron wave-function is excited while the remaining stays in the original band.

Even if this categorization is based on a direct-gap two-band system (top right cartoon in Fig. 10), it can still be applied to complex materials if a theoretical description resorting to a local parabolic two-band approximation

is sufficient to explain the dynamics at play. Figure 11 shows a comparison between the known experiments that employed ATAS or ATRS to study ultrafast charge dynamics below the pump-pulse envelope, using the categorization proposed by Heide and coauthors. For each experiment, the values of the associated relevant parameters are reported in Tab. I. The green star in Fig. 11 (first row in Tab. I) represents the ATAS experiment in SiO_2 performed by Schultze and coworkers and falls into the adiabatic regime, dominated by intraband motion. This regime is in agreement with the observed reversible transient IR-induced polarization, where the 2ω-oscillations originates from strong-field phenomena like Wannier-Stark localization[107]. By reducing the energy gap of the material while keeping almost a constant γ_K (i.e. keeping the pump field intensity in the same range) one would expect to enter into the adiabatic-impulsive Landau-Zener-Stückelberg regime (light orange area in Figs. 10 and 11), characterized by a non-negligible probability for tunnel excitation and a permanent carrier injection into the material CB. This regime has indeed been investigated in 2014 by Schultze and coworkers who applied ATAS to study the ultrafast optical response of Si pumped by an intense few-fs IR pulse[104] (second row in Tab. I, black open circle in Figs. 11). Probing the CB response through the $L_{2,3}$ Si edge, the authors observed a transient signal that does not recover after the pump-probe temporal overlap (left panel in Fig. 12(a)) and orig-

Material	Abs. edge	Δ (eV)	γ_K	γ_a	M	z_R	P_{LZ}
SiO_2[69]	Si $L_{2,3}$	9.00	0.39	9.17	5.66	14.41	0.03
Si[104]	Si $L_{2,3}$	3.40	0.50	2.19	2.19	4.39	0.18
Diamond[92]	-	7.35	3.00	0.13	4.65	1.55	3.0×10^{-10}
GaN[102]	-	3.35	17.67	1.7×10^{-3}	2.09	0.12	5.7×10^{-26}
$GaAs$[105]	As $M_{4,5}$	1.42	0.40	1.36	0.89	2.21	0.56
$Cr{:}Al_2O_3$[103]	-	5.00	4.70	3.7×10^{-2}	3.23	0.69	4.5×10^{-11}
TiS_2[106]	Ti $L_{2,3}$	0.23	2.50	1.4×10^{-2}	0.34	0.14	0.26
SiO_2[94]	-	9.00	1.05	1.33	5.81	5.55	7.2×10^{-5}
Ge[13]	Ge $M_{4,5}$	0.80	0.76	0.22	0.52	0.67	0.54
Diamond[92]	VB to CB	42.00	18.29	2.0×10^{-2}	26.58	1.45	0
SiO_2[94]	VB to CB	29.50	2.54	0.73	19.03	7.51	1.2×10^{-33}

TABLE I. Summary of the adiabaticity parameters for the main ATAS and ATRS experiments that investigate ultrafast charge injection dynamics. All the quantities besides those reported in the last two rows have been calculated by using the minimum direct energy gap at the high symmetry point Γ. The last two rows consider the actual energy gap probed by the XUV photons in the related experiment.

inates from field-induced tunneling across the minimum direct gap. Furthermore, the authors have identified an upper limit of about 450 as for the carrier-induced band-gap reduction and electron-electron scattering time by linking the sub-cycle transient profile of the absorption edge (right panel in Fig. 12(a)) to the number of injected electrons into the CB.

A different interaction regime that allows for permanent carrier injection in the CB, but is based on multiphoton absorption rather than tunneling, should be established when the Keldysh parameter $\gamma_K \gg 1$ (gray area in Figs. 10 and 11). Mashiko and coworkers used an almost 100 times weaker few-fs pulse (intensity of about 10^{10} W/cm^2) to study this regime with ATAS in two wide band-gap materials: GaN[102] (orange full square in Fig. 11) and $Cr{:}Al_2O_3$[103] (violet full triangle in Fig. 11). By probing directly the CB without the need for a resonant inner level, the authors observed fast oscillations of the transmitted spectra which are localized in the region of pump-probe temporal overlap. The period of the oscillations corresponds to integer sub-multiple of the pump IR cycle, highlighting the presence of excitation processes that involve the absorption of an integer number of IR photons. The shortest oscillation period observed in GaN (Fig. 12(b)) corresponds to 860 as, i.e. the absorption of 3 IR photons, while in $Cr{:}Al_2O_3$ the authors observed oscillations with a frequency up to 7ω, largely above 1 PHz. These works suggested the possibility of optically manipulating real carriers in dielectrics beyond the current THz operation limit, setting an important milestone for future high-speed signal processing technologies in the PHz domain[109].

In the last two experiments discussed above, an intuitive picture of the photoinjection process can be achieved with a quantum description of the field ($\gamma_a \ll 1$ in Tab. I), while in the SiO_2 and Si case the field is better thought in classical terms ($\gamma_a > 1$ in Tab. I). When the field description transits from classical to quantum ($\gamma_a \sim 1$), the absorption profile of the material across the gap exhibits a positive tail into the forbidden region, induced above-gap transparency and optical sidebands formation. These features are a direct consequence of the DFKE, an ultrafast non-resonant process based on intraband motion of virtual carriers[99]. ATAS, in combination with wide-gap insulators, offers the possibility to resolve in time this phenomenon[93]. In 2016 Lucchini and collaborators studied the optical response of diamond by probing VB to CB transitions with a 150-as XUV pulse and pumping the sample with a few-fs IR pulse centered around 800 nm. The differential absorption trace shows an oscillating signal that follows the square of the IR field (Fig. 12(c)) and exhibits a V-shaped dispersion in energy[92]. This peculiar phase relation can be explained within a two-band parabolic model[110] and originates from intraband motion, namely DFKE. More recently, Volkov and coworkers used a similar scheme to study the optical response of a 40-nm polycrystalline SiO_2 sample around 30 eV[94]. The resulting ATAS trace shows a rich transient signal that oscillates with twice the pump field frequency and originates from the combined effect of multiple overlapping VB to CB transitions (Fig. 12(d)). The experiment can be reproduced using a DFKE model[110] and an effective band structure that describes the response of fused silica, including randomized orientation and scattering. The model further shows that the apex of the V-shaped structure associated with each individual transition peaks at U_p above the band gap. The branches of the V shape are instead interpreted in terms of interference of Floquet-Bloch states involving absorption of one XUV photon and emission (upper branch)/absorption (lower branch) of two pump photons. The energy spacing of the Floquet-Bloch states determines the aperture (tilt) of the V shape (angle θ in Fig. 12(d)). Furthermore, in the low-intensity regime, the
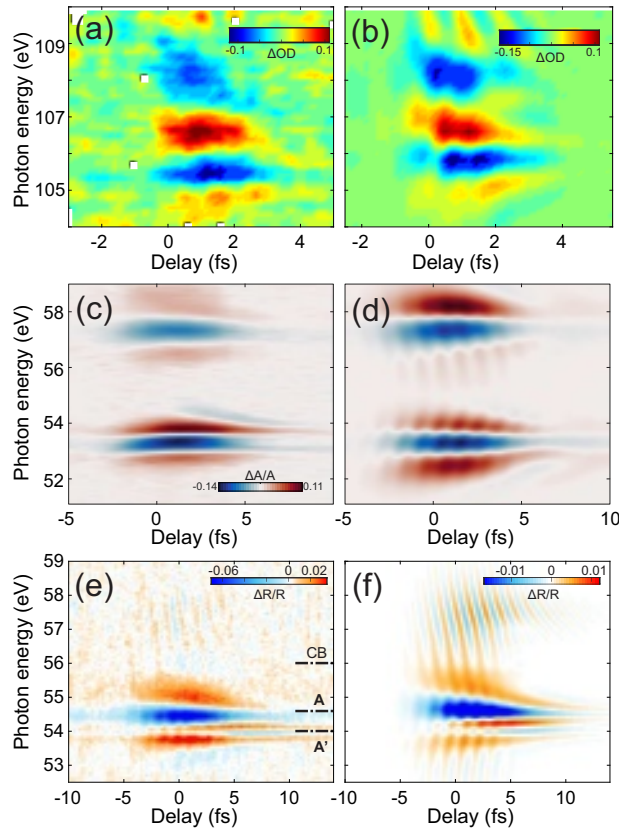
FIG. 6. Experimental, **(a)**, and calculated, **(b)**, transient differential absorption trace of a SiO_2 nanofilm showing an excitonic signature around 106 eV. Experimental, **(c)**, and calculated, **(d)**, transient differential absorption trace retrieved from an ATRS measurement of a MgO crystal. Two transient signals appear at ~ 58 and ~ 60 eV, corresponding to two core-exciton levels that involve a $2p$ Mg hole. Experimental, **(e)**, and calculated, **(f)**, differential reflectivity trace showing the attosecond core exciton response in MgF_2. In addition to the few-fs dynamics, in this case, clear 2ω oscillations are visible also in the experimental results. Panels (a) and (b) are taken from[79] and reprinted with permission from AAAS. Panels (c) and (d) are reprinted with permission from[85], Copyright (2020) by the American Physical Society. Panels (e) and (f) are reproduced from[87]. CC BY 4.0.

DFKE model can be interpreted in terms of third-order susceptibility $\chi^{(3)}$, from which it is possible to extract target specific parameters like the band edges and the electron-hole reduced mass.

When the central photon energy of a strong light pulse becomes comparable to the local energy gap between valence and conduction bands, it might not be possible to frame the interaction in terms of solely real (as in GaN and Cr:Al$_2$O$_3$) or virtual (as in diamond and SiO$_2$) charge dynamics. An early example was reported in 2018 by Schlaepfer and coworkers who used ATAS to study the ultrafast optical response of a 100-nm thick GaAs single crystal, pumped with an 800-nm pulse, and probed at the As M$_{4,5}$ edge at about 41.7 eV[105]. In this case, the direct

energy gap at Γ ($\Delta = 1.42$ eV, see Tab. I) falls within the IR pump spectrum, suggesting a possible dominant role of single-photon excitation. Nevertheless, field effects like intraband motion cannot be excluded due to the strong pump intensity (of about 10^{12} W/cm^2, blue open diamond in Fig. 11). The transient absorption spectrogram (Fig. 12(e)) shows an increased/decreased transmission in the CB/VB region that lasts longer than the pump pulse duration and it is associated with direct charge injection across the energy gap. On top of this relatively slow signal, the ATAS trace shows 2ω oscillations that are confined to the pump-probe temporal region. While both inter- and intraband excitation can cause such a fast modulation of the absorption, their temporal properties differ (right panel in Fig. 12(e)). A comparison of the phase delay of the 2ω oscillations as extracted from the experiment (black curve) and from a two-band model that includes only inter- (green curve) or intraband effects (blue curve), proved that the attosecond timing of the modulations in the CB region is mainly associated to intraband motion. A detailed theoretical analysis of first-principle calculations further showed that intraband motion deeply affects the charge injection mechanism in GaAs, boosting the residual electron population in the CB by almost a factor of three. This injection regime[96], possible only with strong pump pulses, was never observed before and suggested a way of achieving optical control of resonant charge injection on attosecond time scales. It is thus interesting to investigate how it applies to other technologically relevant semiconductors, characterized by a more complex relation between the pump photon energy and the band structure.

Germanium is a remarkable example in this regard. If compared to GaAs, it is characterized by an indirect minimal energy gap ($\Delta_{min} = 0.67$ eV) and a small direct band gap ($\Delta = 0.8$ eV) at which tunnel excitation may be relevant. Nevertheless, there might be other points in the k space, away from Γ, where the VB-CB distance allows for resonant excitation. It is therefore hard to predict a priori which will be the dominant carrier injection mechanism if tunnel injection at Γ (as in the Si case) or single/multiphoton absorption in its proximity. Inzani and collaborators recently used ATRS to study the ultrafast carrier injection in a bulk Ge crystal pumped by a 10-fs IR pulse with peak intensity $I_{IR} = 8 \times 10^{12}$ W/cm^2. They probed conduction and valence band dynamics through excitation from the $3d$ inner levels at ~ 29.5 eV (M$_{4,5}$ edge, see Tab. I). In these experimental conditions, the excitation at Γ should fall into the non-impulsive Landau-Zener regime (green open square in Fig. 11), characterized by a zero net carrier excitation, $N_{exc} = 0$, after the interaction with the pump pulse. Nevertheless, the authors observed transient features in the ATRS trace that increase over time and persist for large values of the pump-probe delay (Fig. 12(f), left panel), a finding that is instead consistent with the excitation of real charges in the CB, as previously observed at longer time scales[74,83]. Like in the GaAs case, the optical response of the ma-
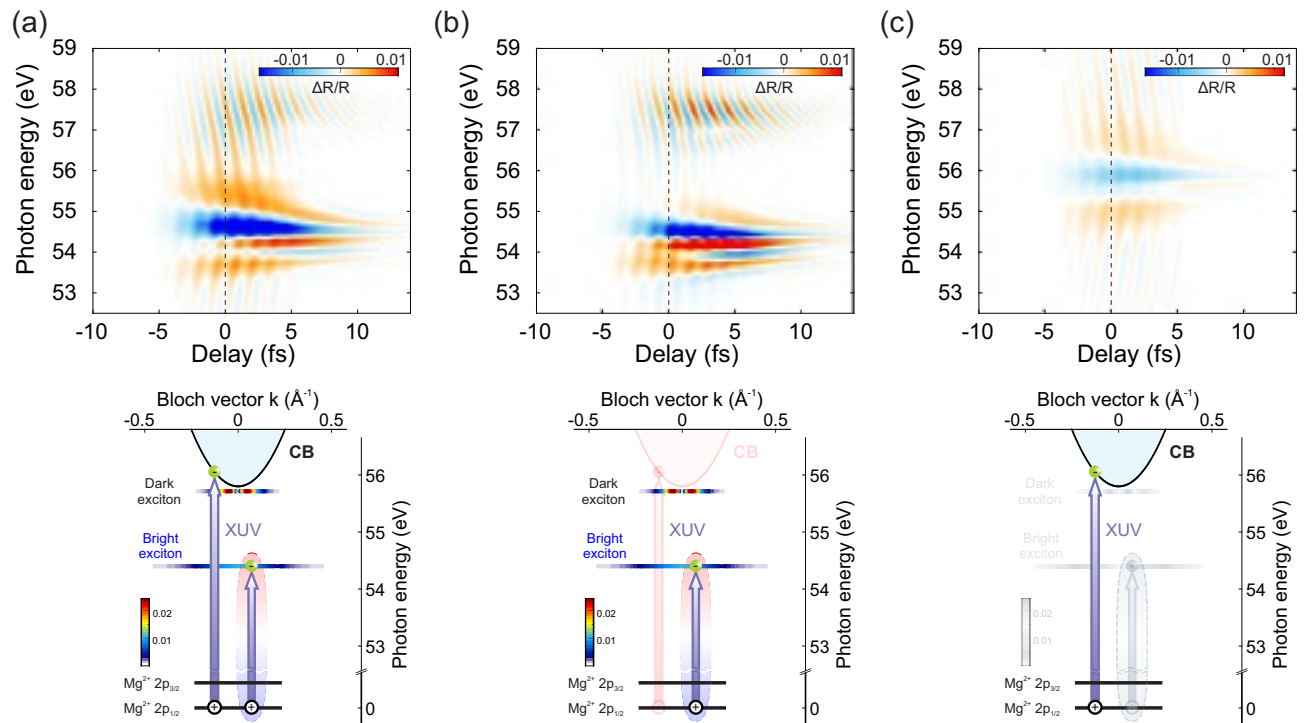
FIG. 7. **(a)**, MgF$_2$ differential reflectivity trace (top panel) calculated with a 1D Wannier-Mott model that includes the Mg 2p states, bright and dark non-dispersive excitonic states and a parabolic conduction band (bottom panel). **(b)**, **(c)** Same quantities but calculated considering only the atomic-like excitonic states or the solid-like crystal bands, respectively[87]. Adapted from[87]. CC BY 4.0.
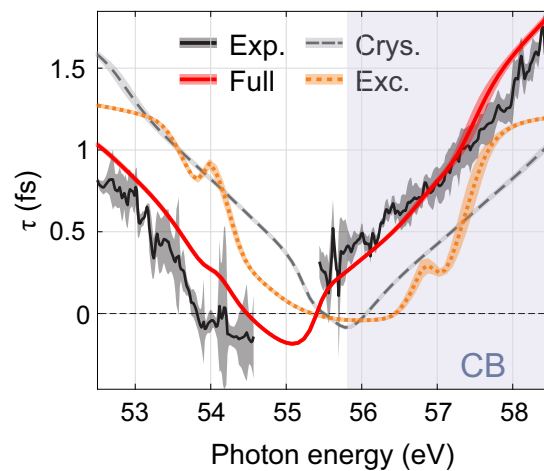
FIG. 8. Phase delay of the oscillating component in the MgF$_2$ ATRS trace of Fig. 6(e). The experimental results, black solid curve, are nicely reproduced by the full model of Fig. 7(a), red solid curve. While the crystal-only contribution, gray dashed curve (model in Fig. 7(c)), shows a similar dispersion but rigidly shifted in energy, the exciton atomic-like contribution, orange dotted curve (model in Fig. 7(b)), fails in reproducing both the timing and the energy dispersion of the oscillations. Adapted from[87]. CC BY 4.0.
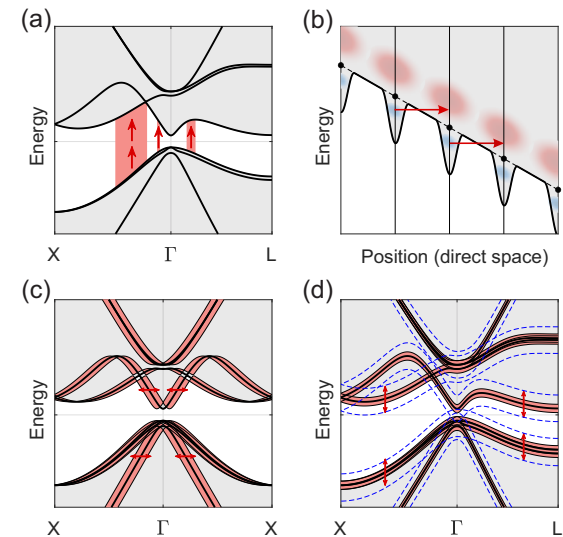
FIG. 9. Cartoon of the main physical phenomena initiated by a strong light-field in solids across the energy gap: **(a)**, vertical charge injection by single- and multi-photon absorption; **(b)**, tunnel excitation; **(c)**, intra-band motion; **(d)**, band dressing and formation of Floquet ladder states (blue dashed curves). Reproduced from[98] with kind permission of Società Italiana di Fisica.
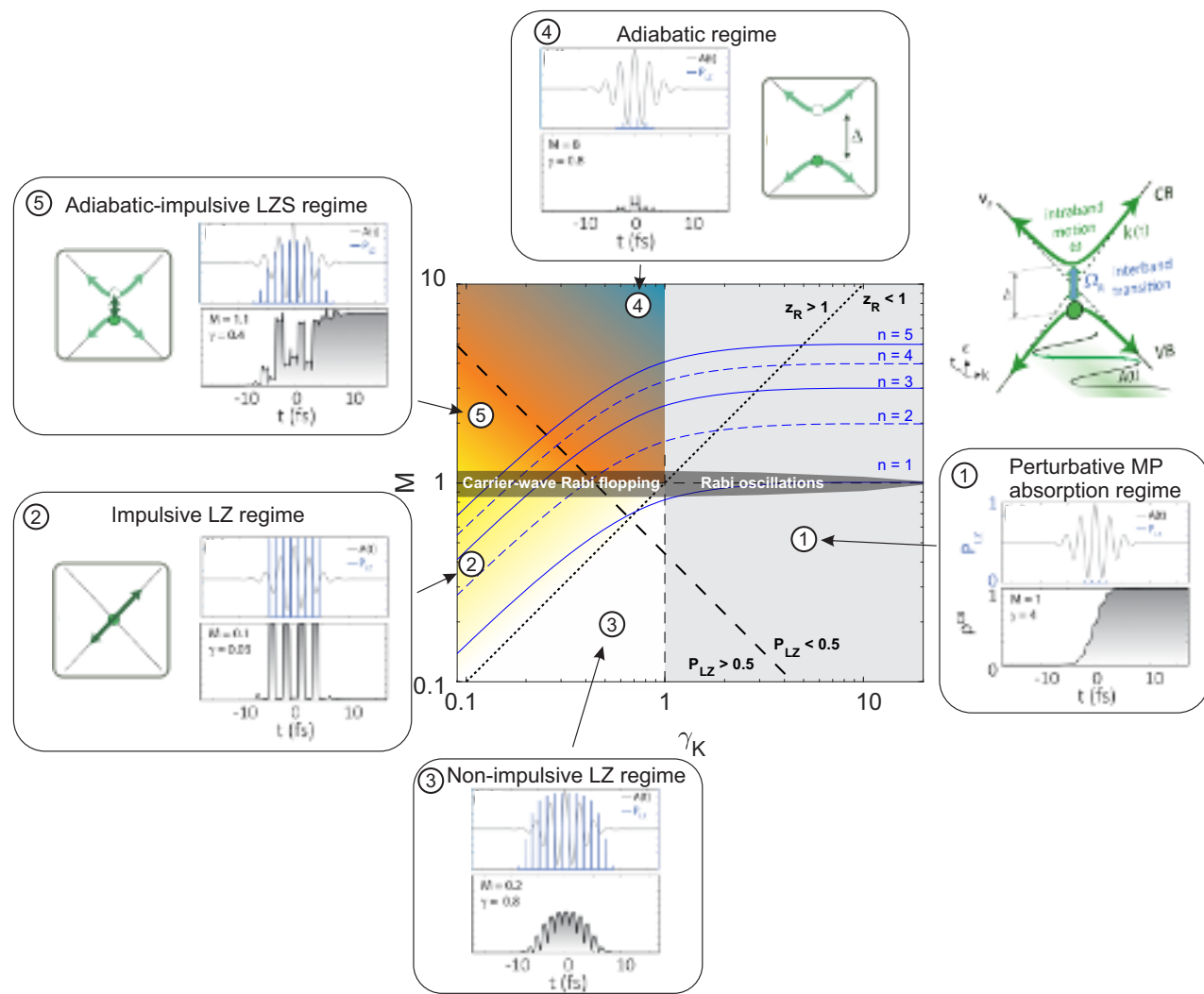
FIG. 10. Map of the interaction regimes individuated by Heide and coworkers[100]: (1) perturbative multiphoton absorption, (2) impulsive Landau-Zener, (3) Non-impulsive Landau-Zener, (4) adiabatic and (5) adiabatic-impulsive Landau-Zener-Stückelberg regime. The five panels present the temporal evolution of the conduction band population ρ^{CB} (black curves) and the Landau-Zener transition probability P_{LZ} (light-blue curves) during the interaction with a 5-fs Gaussian pulse (gray curve). The cartoon on the top-right corner of the main figure shows the parabolic model used. Conduction and valence bands are separated by an energy gap Δ. Their slope defines the Fermi velocity v_F. For relatively weak fields, intraband motion can be neglected and the excitation oscillates with the Rabi frequency Ω_R. For stronger drivers, intraband motion influences interband transitions. Reprinted with permission from[100], Copyright (2021) by the American Physical Society.

terial is further characterized by 2ω oscillations confined in the temporal region of pump-probe overlap, suggesting a non-negligible role of intraband motion and other strong field phenomena. Both the few-fs features and the fast oscillations could be reproduced by time-dependent DFT calculations (Fig. 12(f), right panel) which helped in identifying the carrier excitation mechanisms at play. Figure 13(a) shows the first Brillouin zone of Ge (black frame) and the relevant k points which are characterized by a $N_{exc} \neq 0$ (colored markers) plus the Γ point (black marker). Figure 13(b) displays the square of the pump vector potential while Fig. 13(c) reports the tem-

poral evolution of the normalized electron population for the relevant families of k points of Fig. 13(b) (same color coding). As it is possible to observe, the green and orange points show similar behavior, activating early below the pump pulse envelope and decreasing their contribution around time zero. The yellow and blue points become relevant at later time, after the pump pulse peak, and display an oscillating, out-of-phase behavior. The population at Γ instead follows the IR envelope, going to zero when the pulse is over, as expected from the non-impulsive Landau-Zener regime. As the minimum band gap for the orange and green points matches the
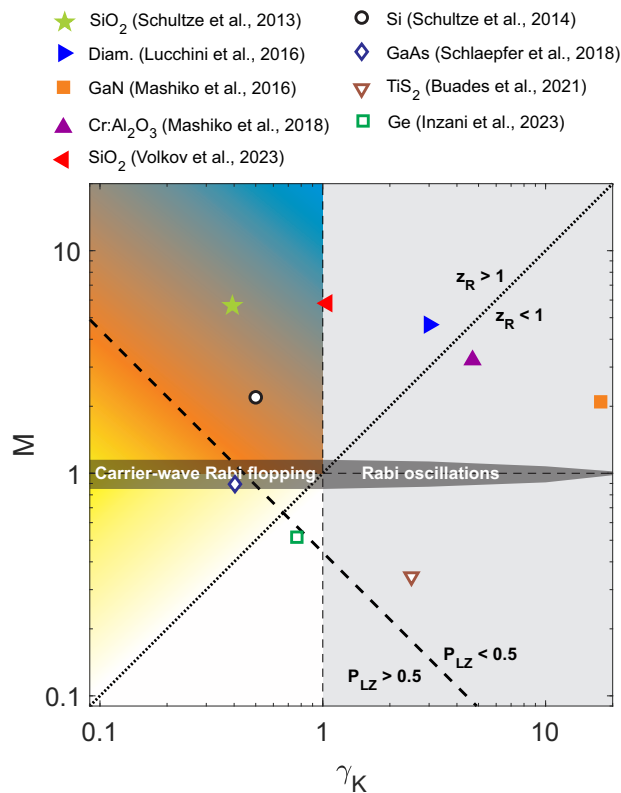
FIG. 11. Comparison between the main experimental works investigating ultrafast carrier injection with ATAS and ATRS as a function of the Keldysh parameter, γ_K, and of the multiphoton parameter, M. The resulting charge injection regime at Γ follows the categories proposed by Heide and coworkers[100]. The black dash-dotted line corresponds to a unitary resonant adiabaticity parameter ($z_R = 1$), while the black dashed line marks points where the Landau-Zener transition probability is $P_{LZ} = 0.5$. Full markers correspond to insulating wide-gap materials (green star: SiO_2[69], blue triangle: diamond[92], orange square: GaN[102], violet triangle $Cr:Al_2O_3$[103], red triangle SiO_2[94]), while open symbols represent experiments with semiconductors or semimetals (black circle: Si[104], blue diamond: GaAs[105], brown triangle: TiS_2[106] and green square: Ge[13]). The values of the corresponding relevant parameters are reported in Tab. I. Reproduced from[13].

IR photon energy (about $1.56\,\mathrm{eV}$) while the blue and yellow points are resonant with two-photon excitation, the different timing of the normalized electron population reported in Fig. 13(c) suggests a complex carrier injection mechanism where one-photon transitions activate earlier during the interaction, to then decrease in favor of two-photon excitation. Interestingly, tunneling does not contribute to the net injection. The authors further performed simulations with a novel theoretical method named dynamical projective operatorial approach (DPOA)[111], which allowed them to increase the sampling in the k space. Refining the identification of the relevant k points they could prove that, under these experimental conditions, charge injection in Ge is domi-

nated by two-photon resonant transitions, and that intraband motion has the opposite effect than in GaAs[105]. By driving the local bands in and out of resonance, it hinders multiphoton excitation and reduces the overall carrier injection into the CB. This first application of ATRS to a semiconductor with sub-cycle resolution thus shows how this spectroscopic technique can be used to deepen our understanding of ultrafast charge dynamics in technologically relevant materials. In tandem with state-of-the-art calculations, it can provide the required knowledge to enable the manipulation of the electronic and optical properties of matter with light on a time scale faster than intra- or inter-valley relaxation and set the basis to extend information technology beyond its current limits.

III. ATTOSECOND TRANSIENT ABSORPTION SPECTROSCOPY - ATAS

The examples reported in the previous sections show that ATAS is a powerful tool for the investigation of ultrafast dynamics in solids. For a deeper understanding of the real capabilities of this all-optical technique, we present here its basic principles, strengths and limitations.

A. Principle of the technique

In its easiest description, the absorption of photons of energy $\hbar\omega$ into a material is governed by the Beer-Lambert law, which defines the relationship between the intensity of the incident, $I_0(\omega)$, and transmitted, $I_t(\omega)$, light through the sample:

$$I_t(\omega) = I_0(\omega)e^{-\alpha(\omega)L} = T(\omega)I_0(\omega), \qquad (1)$$

where $T(\omega) = e^{-\alpha(\omega)L}$ is the transmission of the sample, L is its thickness, and $\alpha(\omega)$ its absorption coefficient. This latter can be expressed in terms of the speed of light, c, and the imaginary part of the complex refractive index of the material, $\tilde{n}(\omega) = n(\omega) + ik(\omega)$:

$$\alpha(\omega) = 2\frac{\omega}{c}k(\omega). \qquad (2)$$

Given that the refractive index of the material is equal to the square root of the complex dielectric function, $\varepsilon(\omega) = \varepsilon_1(\omega) + i\varepsilon_2(\omega)$, the absorption coefficient can be equivalently written as:

$$\alpha(\omega) = 2\frac{\omega}{c}\frac{\varepsilon_2(\omega)}{|\varepsilon(\omega)|}\sqrt{\frac{|\varepsilon(\omega)| - \varepsilon_1(\omega)}{2}}. \qquad (3)$$

Within this picture, the absorption of incident photons inside the target is entirely described by the absorption coefficient α, which reflects the microscopic interaction of light with the basic constituents of matter (electrons, spin, lattice). Nevertheless, as the quantity usually measured is the transmission, T, the absorption properties
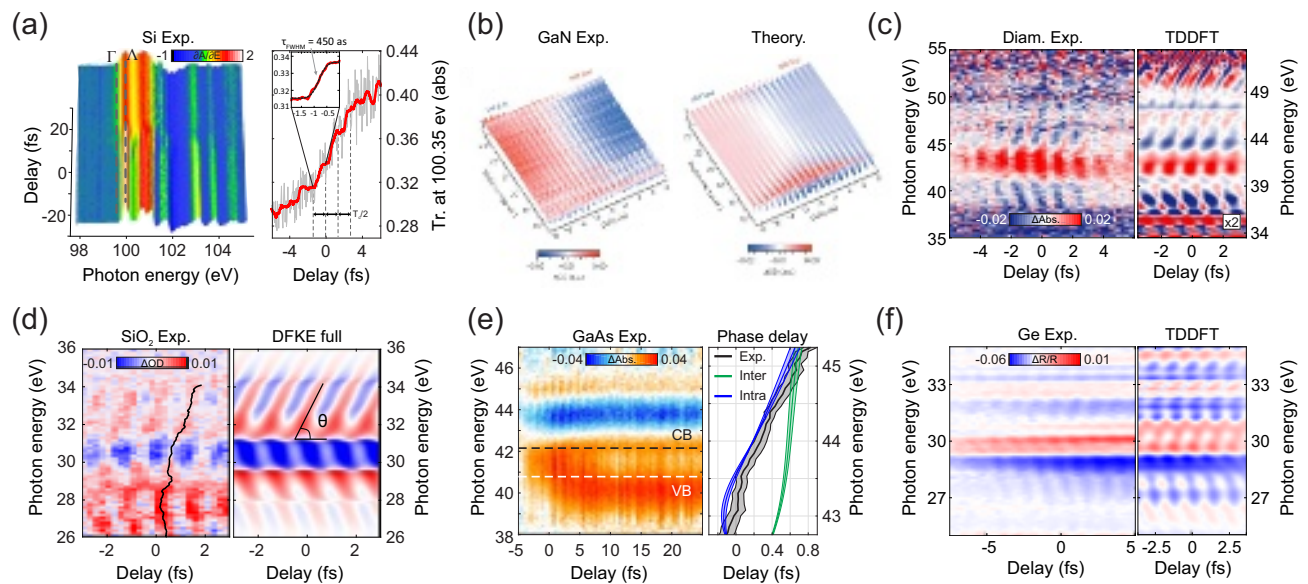
FIG. 12. **(a)** Energy derivative of the measured XUV absorbance of a Si pellicle, $\partial Abs/\partial E$, plotted as a function of probe-photon energy E_{XUV} and time delay between pump and probe pulses[104]. The right panel reports the temporal evolution of the XUV transmission ($T = 10^{-Abs}$) at 100.35 eV (gray, raw signal, red, rolling average), which exhibits a step-like increase synchronized with the laser electric field oscillations. The inset shows the fit used to evaluate the step rise time. **(b)** Left panel, ATAS trace of a 102-nm-thick GaN sample[102]. The trace shows the deviation of optical density (ΔOD) with and without the pump pulse as a function of the temporal delay. Right panel, transient interband polarization simulated with a multilevel optical Bloch equation[108]. **(c)** Experimental (left) and simulated (right) pump-induced relative changes in the absorbance of a 50-nm thick polycrystalline diamond sample[92]. **(d)** Experimental transient absorption spectra of a 40-nm thick polycrystalline SiO_2 film as measured (left) and calculated with a model based on the DFKE (right)[94]. The black curve in the left panel shows the phase delay of the 2ω oscillations obtained by Fourier filtering the spectrogram, while the quantity θ on the right indicates the opening of the V-shaped structure. **(e)** Transient absorption trace of a 50-nm thick GaAs single crystal[105]. The right panel shows the phase delay of the 2ω oscillations in the CB region as extracted from the experiment (back curve) and calculations that consider only intra- (blue) and interband (green) transitions. **(f)** Measured (left) and calculated (right) differential reflectivity trace, $\Delta R/R$, of a single Ge crystal pumped with a few-fs IR pulse at the critical angle for total external reflection ($66°$)[13]. Panel (a) is adapted from[104] and reprinted with permission from AAAS. Panel (b) is reprinted by permission from Springer Nature Customer Service Centre GmbH: Nature[102]. Copyright (2016). Panel (c) is from[92]. Reprinted with permission from AAAS. Panel (d) is reprinted from[94]. CC BY 4.0. Panel (e) is reprinted by permission from Springer Nature Customer Service Centre GmbH: Springer Nature, Nature Physics,[105], Copyright ©2018, The Author(s). Panel (f) is reprinted by permission from Springer Nature Customer Service Centre GmbH: Springer Nature, Nature Photonics,[13], Copyright ©2023, The Author(s).

are often represented by the absorbance (also called optical depth):

$$\text{Abs}(\omega) = \alpha(\omega)L = -\ln(T) = \ln\left(\frac{I_0(\omega)}{I_t(\omega)}\right), \quad (4)$$

or, equivalently, by the optical density:

$$\text{OD}(\omega) = -\log_{10}(T) = \log_{10}\left(\frac{I_0(\omega)}{I_t(\omega)}\right). \quad (5)$$

Figure 14(a) shows the absorption profile of Si in the region between 80 and 200 eV[112]. At these energies, the absorption coefficient of Si presents a well-defined rise (called absorption edge) around 99.62 eV[113] (marked with $L_{2,3}$ in Fig. 14(a)). This behavior is common to all the materials and it is observed every time that a new transition from an inner level up to the first unoccupied states becomes energetically possible. In X-ray spectroscopy, the different absorption edges are classified depending on the shell of the initial electronic state, i.e., K-, L-, M-edges correspond to transitions from the 1st, 2nd, 3rd shell respectively. While photons in the visible-infrared (VIS/IR) region of the spectrum allow for electronic transitions from the valence to the conduction bands of a solid, XUV or soft X-ray (SXR) radiation is capable of reaching the inner electronic shells of the material, thus gaining element-specificity. In the example of Fig. 14(a), the $L_{2,3}$ edges involve the ionization of a Si $2p$ state. It is important to notice that not all edges are sharp. If a close upper level is available in the same shell, then the hole created by the XUV can decay by a fast Auger process mediated by a Coster-Kronig transition, and the edge appears to be shallow. This is the case for the Si L_1 edge, at about 150 eV, which originates from a $2s$ core hole (Fig. 14(c)). The sharp or shallow nature of an edge has important im-
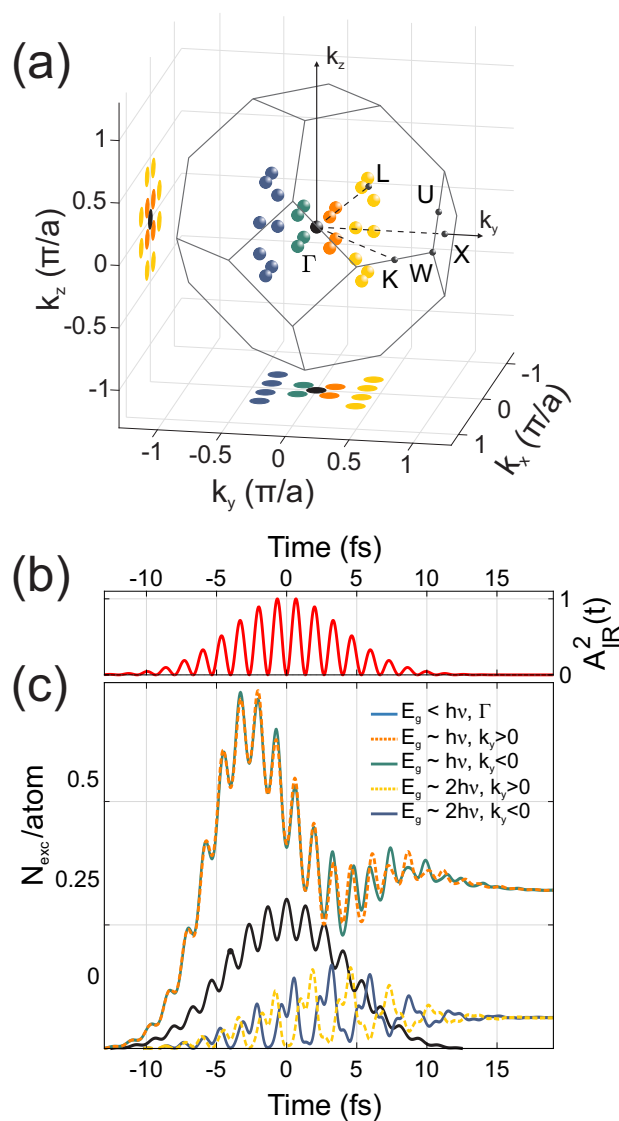
FIG. 13. **(a)** Points in the first Brillouin zone of Ge which are found to participate to the residual carrier injection in the experimental conditions of Ref.[13]. The black dot is located at the Γ point. Orange and green dots represent a family of points where the first energy gap is resonant with one pump photon, while the minimum gap at the blue and yellow points is two-photon resonant. **(b)** Time evolution of the square of the pump vector potential. **(c)** Excited electron population computed by time-dependent DFT at the selected k-points (same color coding as in (a)) and normalized by the number of k-points of the same family. Reprinted by permission from Springer Nature Customer Service Centre GmbH: Springer Nature, Nature Photonics,[13], Copyright ©2023, The Author(s).

plications for its probing capabilities. As an example, Fig. 14(b) shows the relative change of the absorption coefficient, $\Delta\alpha/\alpha = (\alpha' - \alpha)/\alpha$, obtained by imagining that the only effect of the pump is to produce a rigid energy shift of the absorption profile $\alpha'(\omega) = \alpha(\omega - \bar{\omega})$ with
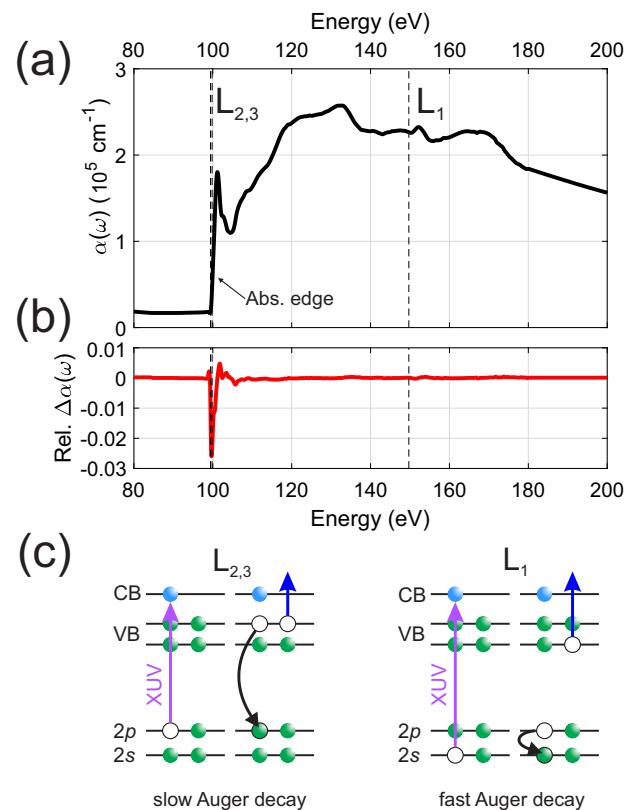

FIG. 14. **(a)** Absorption coefficient of Si around its $L_{2,3}$ edges. Data were taken from[112]. **(b)** Relative change in the absorption profile originating from a 10-meV rigid energy shift of the coefficient α in (a). **(c)** Auger decaying mechanisms dictating the lifetime of the core hole involved in the L edges of Si.

$\bar{\omega} = 10\,\text{meV}$. As it is possible to observe, this produces a $\Delta\alpha/\alpha$ of about 3% around the $L_{2,3}$ edge, while the L_1 edge is almost unchanged.

The broadband spectrum typical of the attosecond sources, generally allows for probing a wide range of energies around the absorption edge. According to nomenclature from X-ray spectroscopy, the region of the absorption spectrum in the vicinity of the edge and up to $10-15\,\text{eV}$ above it, is called XANES (X-ray Absorption of Near-Edge Structure). It allows to probe the electronic occupation of the states lying in the CB[114,115]. Above the XANES region, electrons are directly emitted in the continuum, where they scatter with the electron density on the surrounding atoms: this region is called EXAFS (Extended-edge X-ray Absorption Fine Structure). In this region, the scattering process is energy-dependent and modulates the absorption probability, producing an interference pattern from which the interatomic distances can be retrieved[114].

The possibility of directly probing the electronic occupation of a solid led many research groups to extend the XUV absorption spectroscopy technique to time-resolved experiments in a pump-probe fashion. As discussed in
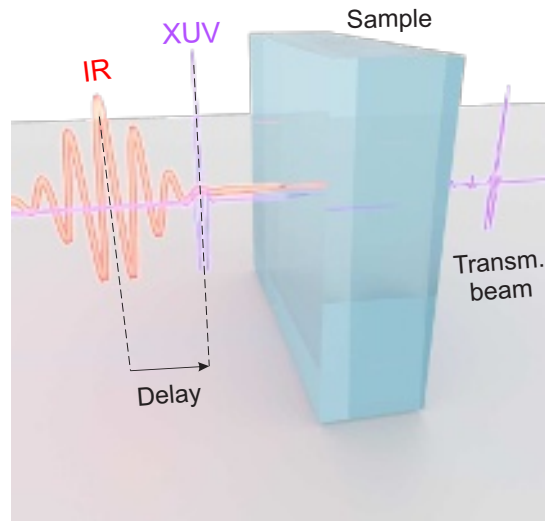
FIG. 15. Schematic of an ATAS experiment: a few-fs IR pulse perturbs the system initiating the a dynamics which is probed by the transmitted XUV attosecond radiation while varying their relative delay.

the previous section, in a typical ATAS experiment the system under investigation is excited with a VIS/NIR few-cycle pump pulse (usually the same pulse driving the HHG process), triggering ultrafast electron dynamics which are subsequently probed by the attosecond XUV broadband pulse (Fig. 15). The probe light transmitted through the target is then collected with a spectrometer. In order to detect pump-induced changes in the absorbance of the material, a series of pump-on/pump-off spectra (i.e., with or without exciting the sample with the pumping radiation) are collected for different values of the delay, τ, between the pulses. This allows one to compute the differential absorbance, defined as:

$$\begin{aligned}\Delta\text{Abs}(\omega,\tau) &= \text{Abs}'(\omega,\tau) - \text{Abs}(\omega) = \\ &= (\alpha'(\omega,\tau) - \alpha(\omega))\, L = \\ &= \ln\left(\frac{I_t(\omega)}{I_t'(\omega,\tau)}\right),\end{aligned} \tag{6}$$

where Abs', α', I_t' are, respectively, the absorbance, the absorption coefficient, and the transmitted intensity of the pumped material. We note that the pump-probe scheme in ATAS can be reverted for the case of XUV-induced dynamics, as for the core-excitonic dynamics[79,85,87] discussed in Sec. II B.

Whether the chosen observable is absorption or transmission, its sensitivity with respect to a relative change in the real and imaginary parts of $\tilde{n}$ and ε can be estimated by calculating the sensitivity functions[116]:

$$S_f^{(F)} = \left(\frac{f}{F}\right)\left(\frac{\partial F}{\partial f}\right), \tag{7}$$

where f equals n, k, ε_1 or ε_2, while $F = \text{Abs}$ or T. For example, $S_n^{(\text{Abs})}$ is the sensitivity of the absorbance to the real part of the material refractive index. In this way, the pump-induced relative change of the chosen observable F can be written as:

$$\begin{aligned}\frac{\Delta F}{F} &= S_n^{(F)}\frac{\Delta n}{n} + S_k^{(F)}\frac{\Delta k}{k} \\ &= S_{\varepsilon_1}^{(F)}\frac{\Delta\varepsilon_1}{\varepsilon_1} + S_{\varepsilon_2}^{(F)}\frac{\Delta\varepsilon_2}{\varepsilon_2}.\end{aligned} \tag{8}$$

Starting from Eqs. (2) and (4), it is trivial to show that if $F = \text{Abs}$, then $S_n^{(\text{Abs})} = 0$ and $S_k^{(\text{Abs})} = 1$. The sensitivity with respect to the real and imaginary part of ε are instead given by:

$$S_{\varepsilon_1}^{(\text{Abs})} = -\frac{\varepsilon_1}{2|\varepsilon|}$$

$$S_{\varepsilon_2}^{(\text{Abs})} = \frac{\varepsilon_2^2}{2|\varepsilon|\,(|\varepsilon| - \varepsilon_1)}. \tag{9}$$

Figures 16(a) and 16(b) show the absolute value of the absorbance sensitivity functions of Ge around its $M_{4,5}$ edge. Figures 16(c) and 16(d) report instead the values of the sensitivities for the transmission of a 50-nm thick Ge sample, which are given by:

$$\begin{aligned} S_n^{(T)} &= 0 \\ S_k^{(T)} &= -\text{Abs} \\ S_{\varepsilon_1}^{(T)} &= \frac{\omega L}{c}\frac{\varepsilon_2}{|\varepsilon_2|}\frac{\varepsilon_1\sqrt{|\varepsilon| - \varepsilon_1}}{\sqrt{2}|\varepsilon_1|} \\ S_{\varepsilon_2}^{(T)} &= -\frac{\omega L}{c}\frac{\varepsilon_2}{|\varepsilon_2|}\frac{\varepsilon_2^2}{\sqrt{2}|\varepsilon|\sqrt{|\varepsilon| - \varepsilon_1}} \end{aligned} \tag{10}$$

Both Abs and T are hence sensitive only to the imaginary part of $\tilde{n}$ and to both the real and imaginary part of ε. Nevertheless, for those materials that can be described by the Lambert-Beer law, the absorption is usually dictated by ε_2, as highlighted by $|S_{\varepsilon_2}| > |S_{\varepsilon_1}|$ for both T and Abs. It is worth noting that even if the sensitivities for the transmission scale linearly with the sample thickness, T decreases exponentially with an increasing L, possibly hindering detection (see Figure 17 and the related discussion). To conclude, we would like to underline that even if the static transmittance is in general affected by the reflection at the vacuum-solid interfaces of a finite sample, thin-film effects are less severe in the XUV spectral region[117,118]. ATAS experiments are usually performed at angles close to normal incidence, where the XUV reflectivity is minimized, while ATRS gives an appreciable signal only close to the critical angle for total external reflection, θ_c (see Sec. IV). Since typically $\theta_c \gg 0°$ in the XUV, the contribution to ATAS of any dynamical change in the sample surface reflectivity is, to a first approximation, negligible.
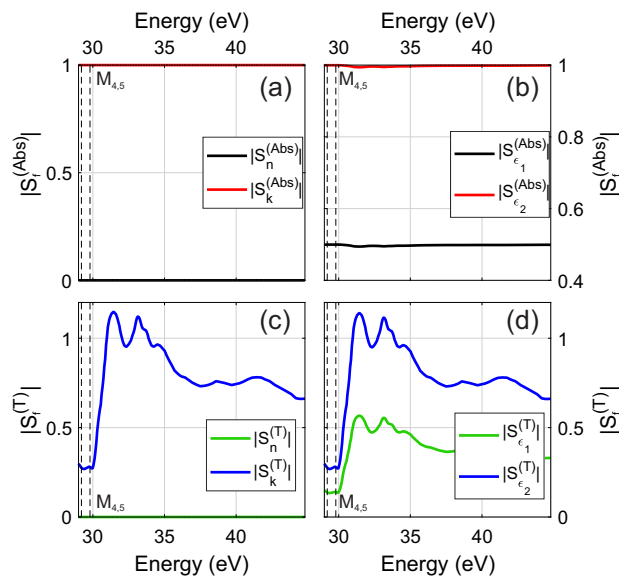
FIG. 16. Ge absorbance sensitivity functions with respect to the real and imaginary part of $\tilde{n}$, **(a)**, and ε, **(b)** around the $M_{4,5}$ edge. **(c)** and **(d)** report the same sensitivities but calculated for the transmission T of a 50-nm Ge sample. All the quantities have been derived by using the complex refractive index reported in Ref.[84].

B. Strengths and limitations

In X-ray absorption spectroscopy, the most direct link between $\alpha(\omega)$ and the electronic band occupation of the material is obtained when performing measurements at a K-edge (i.e., transitions from the first core-shell). In this case, as demonstrated by Sidiropoulos and coworkers[119], the absorbance profile can be immediately fitted by a function that contains the electronic density of states (DOS) and, for an electronic system at equilibrium, a Fermi-Dirac distribution at the given electron temperature. However, most of the K-edges of the elements in the periodic table are inaccessible to conventional HHG-based laser sources (see Sec. V C). For this reason, besides the work by Sidiropoulos et al., all the ATAS investigations performed so far have studied the ultrafast response of the excited target at L-[69,79,104,106], M-[13,73,81,105], or N-edges[120–122]. However, all these edges present a multiple-edge structure due to the spin-orbit splitting of the related core levels, producing an energy separation of the order of a few eVs or less. As a consequence, the total absorbance of the material can be composed of multiple, overlapping edges, making the interpretation of ATAS data a non-trivial task. Fortunately, the direct relation between the absorption coefficient and the imaginary part of the complex refractive index of the material gives the possibility to disentangle individual contributions to the total sample absorbance, like in the work by Zürch et al.[73], where carrier relaxation dynamics in Ge have been studied after disentangling the two

overlapping contributions originated by transitions from the $3d_{3/2}$ and $3d_{5/2}$ states, responsible for the $M_{4,5}$ edge around 30 eV. While the presence of multiple edges in ATAS thus does not constitute a severe limitation, we will discuss in the next section how this changes for transient reflectivity measurements.

ATAS, or in general any kind of absorption-based measurement, is known to be a bulk-sensitive spectroscopic technique. A first consequence of this property is that absorption spectra exhibit a low sensitivity to sample inhomogeneity and impurity, because the total response is averaged over the whole volume of the probed material. Furthermore, the technique is also poorly sensitive to the surface quality of the sample. This may be seen as an advantage, since surface roughness as well as contamination of the surface layer would not greatly affect the overall absorption of the material. While in general allowing for an easier fabrication and preparation of the samples surfaces (a great advantage with respect to reflectivity measurements), the bulk sensitivity poses some serious limitations on the sample thickness. As in ATAS pump and probe pulses have considerably different photon energies, the two colors will propagate inside the material with different group velocities. If the sample is too thick, the total delay accumulated between the two pulses can be comparable to the typical time scale of the dynamics under investigation, possibly hindering its correct observation. Nevertheless, the most severe limitation on the sample thickness comes from the strong light-matter interaction in the XUV/SXR energy range. By considering the exponential decay given by Eq. (1), one obtains that the transmitted light intensity drops by roughly 70% already in the first 100–150 nm for almost any kind of material. As a direct consequence, it is extremely hard to study samples thicker than ~ 200 nm with ATAS because not enough photons will be transmitted. At the same time, if the sample is too thin (e.g. a monolayer), the absorbance gets smaller and eventually negligible compared to that of the substrate. While in static experiments this condition might still be acceptable, detecting pump-induced signals for very thin samples could constitute a rather challenging task.

As an example, Fig. 17(a) reports the change in absorbance of Si, caused by a 10-meV rigid energy shift of its absorption profile around the L edges (the associate $\Delta\alpha/\alpha$ is plotted in Fig. 14(b)). To get a ΔAbs of the order of a few percent (the typical minimum value that can be detected), the sample thickness needs to be in the hundreds of nm range. The associated transmission T, though, quickly decreases as $\Delta\alpha$ increases (Fig. 17(b)). Figure 17(c) shows an energy cut around the maximum value of ΔAbs, located at 100.4 eV, just after the $L_{2,3}$ edges. To observe a change in absorbance of the same amplitude as the associated change in α (i.e. 3%, see Fig. 14(b)), the sample needs to be almost 238-nm thick, with a transmission of only 7% (light blue dashed curve in Fig. 17(c)). Therefore a good balance between maximizing $\Delta\alpha$ while maintaining a reasonable photon flux
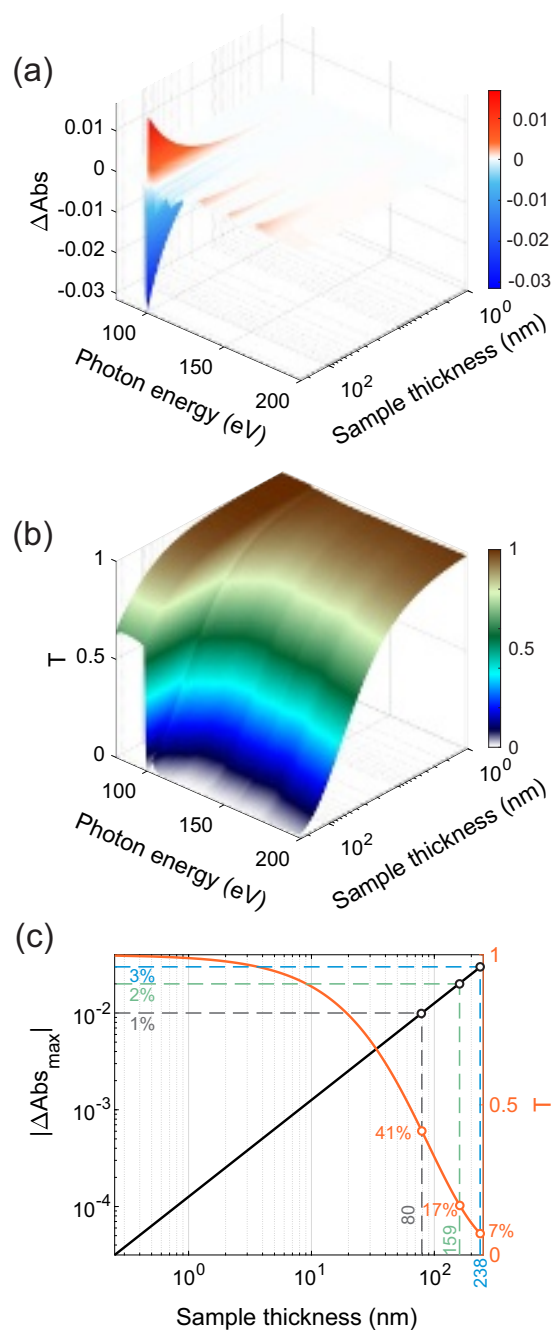
FIG. 17. **(a)** Changes in the absorbance of Si, ΔAbs, around the L edges, originating from a rigid 10-meV energy shift of the absorption profile of Fig. 14(a), and plotted as a function of energy and sample thickness. **(b)** Associated transmittance T. **(c)** Energy cut at the position of the local absorption maximum in the proximity of $L_{2,3}$ Si edge (i.e. at 100.4 eV).

on the detector should be carefully considered.

The above example also underlines a lower limit to the sample thickness L. As further discussed in Sec. V A, the usual experimental noise floor in attosecond spectroscopy ranges around the 1% level. To get a variation

of $\Delta\alpha = 0.01$, around the $L_{2,3}$ Si edge, i.e. the best case, 80 nm of material are needed (Fig. 17(c), gray dashed curve). This simple example suggests that the use of ATAS to investigate electron dynamics in very thin samples approaching the few-layer thickness might be of difficult, if not impossible, implementation. Nevertheless, we would like to stress that the results obtained in this analysis are strictly dependent on the specific sample under investigation (in particular, its absorption coefficient in the chosen energy range) and the amplitude of the simulated dynamics. Considering a material with higher absorption or larger pump-induced modification of its optical properties, as for the case of strong-field excitation regimes, could result in detectable ATAS signals for sample thicknesses down to a few tens of nm (see examples in Sec. II C).

To conclude, current ATAS experiments are limited to a relatively narrow range of sample thickness, from a few tens to a few hundreds of nm (typically up to ~ 200 nm). This has two main drawbacks: (i) high-quality samples are not easily available with the required thickness and, (ii) heat dissipation is not efficient. The latter constitutes one of the main limitations of the technique. The poor stability of standard high-harmonic sources and the slow detection systems available, often force the use of high-intensity pumps, close to the material damage threshold, to obtain detectable signals of the order of ΔAbs ≥ 0.01 and overcome the noise floor. This badly matches the requirement for thin, free-standing samples, which cannot easily dissipate the deposited thermal energy (see Sec. V A). Unwanted effects like thermal-induced accumulated damage, or heat-induced artifacts in the absorption spectrum (see the work of Zürch et al.[73] for a clear example) can affect ATAS experiments for much lower pump intensities than for the case of bulk samples. In some cases, this problem has been solved by reducing the laser repetition rate below the kHz, to be able to perform the experiment (e.g, Ref.[76]). Therefore, unless accompanied by a noise level reduction (see Sec. V A), the current tendency to increasing the repetition rate of the high-harmonic sources (see Sec. V C) might not be beneficial, or even negatively impact the study of strong-field phenomena with ATAS.

IV. ATTOSECOND TRANSIENT REFLECTION SPECTROSCOPY - ATRS

While potentially carrying the same information, in certain cases the light reflected by a sample may be a better probe than its transmitted counterpart. In the following, we introduce the principles of ATRS, discussing in detail its strengths and weaknesses.

A. Principle of the technique

A correct interpretation of the transient optical properties of a system out of equilibrium stems from a detailed knowledge of its equilibrium (or static) properties. In ATAS, the sample is usually placed at normal incidence and does not modify the beam path of the attosecond radiation. The static absorption can thus be measured with relatively high precision by moving the sample in and out the beam path and acquiring the incoming, $I_0(\omega)$, and transmitted, $I_t(\omega)$, spectra in close sequence to obtain the equilibrium transmission $T_0(\omega) = I_t(\omega)/I_0(\omega)$. Ideally, one would follow the same approach in reflectivity measurements, where the static reflectivity is given by the ratio between the reflected and incident beam intensities, $R_0(\omega) = I_r(\omega)/I_0(\omega)$. Nevertheless, ATRS experiments are performed with a finite incidence angle, θ_{in}, with respect to the surface normal (Fig. 18). Therefore, removing the sample would deviate the path of the incoming radiation, rendering the direct detection of $I_0(\omega)$ impossible unless a complex XUV spectrometer capable to be precisely moved in vacuum is employed. An alterna-
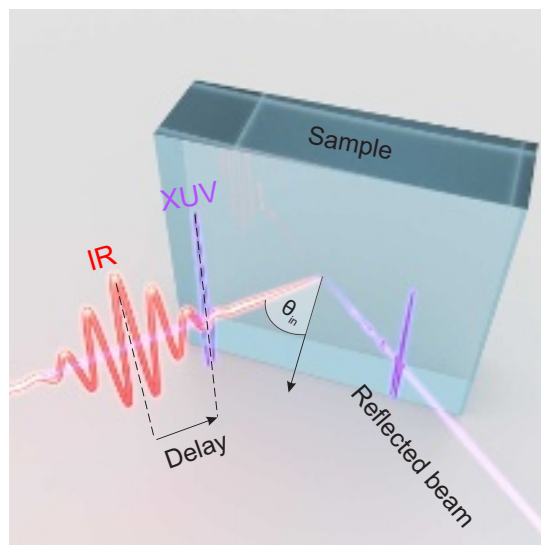

FIG. 18. Schematic of an ATRS experiment: a few-fs IR pulse induces a perturbation of the system which is probed by the reflected XUV attosecond radiation while varying their relative delay. In this case, the incident angle θ_{in} is usually different from zero.

tive approach consists in collecting, in addition to the reflected beam intensity $I_r(\omega)$, also the radiation reflected from a calibrated sample, $I_{cal}(\omega)$, subsequently placed in the same position and with the same angle θ_{in}. This approach is simpler to implement as it is usually possible to place both the calibration and unknown samples close by on the same holder[91]. To further reduce the required movements and associated possible measurement errors, the calibration material can be deposited on a portion of the unknown sample area[87]. Following this approach,

the sample static reflectivity is thus given by:

$$R_0(\omega) = \frac{I_r(\omega)}{I_{cal}(\omega)} R_{cal}(\omega), \tag{11}$$

where R_{cal} is the known absolute reflectivity of calibration sample, which can be computed from its complex refractive index.

From a theoretical perspective, both the reflection and absorption of light incident onto an interface between two different optical media is generally described by the Fresnel equations. Derived for a macroscopic system at equilibrium, they have been found to hold also at extreme temporal and spatial scales[123]. They define the relationship between the incident, reflected and transmitted electric fields at the interface, as a function of θ_{in} and the complex refractive indices of the two media, $\tilde{n}_1$ and $\tilde{n}_2$. Considering the case of s-polarized light, the fraction of light intensity that is reflected at the interface, R_s, can be written as:

$$R_s = |r_s|^2 = \left| \frac{\tilde{n}_1 \cos(\theta_{in}) - \tilde{n}_2 \cos(\theta_{tr})}{\tilde{n}_1 \cos(\theta_{in}) + \tilde{n}_2 \cos(\theta_{tr})} \right|^2, \tag{12}$$

where r_s is the Fresnel coefficient for the reflected s-polarized light, and θ_{tr} is the angle of transmission. Using the well known Snell equation $\tilde{n}_1 \sin(\theta_{in}) = \tilde{n}_2 \sin(\theta_{tr})$ and treating a vacuum-solid interface (i.e. $\tilde{n}_1 = 1$) we can write:

$$R_s = \left| \frac{\cos(\theta_{in}) - \sqrt{\tilde{n}_2^2 - \sin(\theta_{in})^2}}{\cos(\theta_{in}) + \sqrt{\tilde{n}_2^2 - \sin(\theta_{in})^2}} \right|^2. \tag{13}$$

For p-polarized light, the reflectivity in vacuum is instead given by:

$$R_p = |r_p|^2 = \left| \frac{\sqrt{\tilde{n}_2^2 - \sin(\theta_{in})^2} - \tilde{n}_2^2 \cos(\theta_{in})}{\sqrt{\tilde{n}_2^2 - \sin(\theta_{in})^2} + \tilde{n}_2^2 \cos(\theta_{in})} \right|^2. \tag{14}$$

The above equations assume the two optical media to be homogeneous and isotropic, while the surface is supposed to be infinitesimally thin and flat. If the latter is not the case, the surface roughness can be considered by introducing a correction term called the Debye-Waller factor $e^{-\sigma^2 q^2}$, which models light attenuation due to scattering processes at the interface characterized by a roughness σ and a scattering vector $q = 4\pi\lambda \sin(\theta_{in})$[124].

The direct relationship between R_s (R_p) and the complex refractive index of the material, $\tilde{n}_2(\omega)$, suggests the possibility of accessing the physical quantities describing the optical response of the sample through reflectance measurements. However, the phase information on the Fresnel reflection coefficient is lost while measuring R_s, rendering impossible a direct inversion of Eq. (13) to extract both the real and imaginary part of $\tilde{n}_2$. If the reflectivity of the material is known on a broad energy range,

a possible solution consists in writing $r_s = \sqrt{R_s}e^{i\phi}$, and apply the KK relations to obtain the pseudo-phase[86]:

$$\phi(\omega) = \frac{1}{\pi}\int_0^\infty \ln\left|\frac{\omega'+\omega}{\omega'-\omega}\right|\frac{d\ln\{R_s(\omega')\}^{\frac{1}{2}}}{d\omega'}d\omega', \quad (15)$$

from which the real and complex part of $\tilde{n}_2$ can be computed. Unfortunately, this approach requires knowing the reflectivity of the sample in the whole positive frequency axis, as truncating the integral in Eq. (15) may introduce artifacts. When this is not possible, an alternative route consists of collecting reflectance spectra at different angles of incidence and applying a fitting procedure based on Eq. (13) to have a well-posed mathematical problem. Multi-angle reflectivity measurements are indeed commonly performed to characterize the optical response of the material in various spectral regions, from the VIS/NIR up to the XUV range. A clear example is the study performed by Kaplan et al. to extract the complex refractive index of germanium at energies covering the $M_{4,5}$ absorption edge[84].

In ATRS, the transient changes induced in the optical properties of the material by the pump are probed by collecting the reflected attosecond radiation while scanning the relative delay between the pulses. The results are often reported in terms of differential reflectivity, defined as:

$$\frac{\Delta R}{R} = \frac{R'(\omega,\tau) - R_0(\omega)}{R_0(\omega)}, \quad (16)$$

where R' is the reflectivity of the pumped material. As discussed for the absorbance and transmission, $\Delta R/R$ can be equivalently written using the sensitivity functions:

$$\begin{aligned}\frac{\Delta R}{R} &= S_n^{(R)}\frac{\Delta n}{n} + S_k^{(R)}\frac{\Delta k}{k} \\ &= S_{\varepsilon_1}^{(R)}\frac{\Delta\varepsilon_1}{\varepsilon_1} + S_{\varepsilon_2}^{(R)}\frac{\Delta\varepsilon_2}{\varepsilon_2},\end{aligned} \quad (17)$$

which can be calculated as:

$$S_f^{(R)} = \frac{f}{R_s}\frac{\partial R_s}{\partial f} = 2\frac{f}{R_s}\Re\left\{r_s^*\frac{\partial r_s}{\partial f}\right\}, \quad (18)$$

where r_s^* is the complex conjugate of r_s and f is either n, k, ε_1 or ε_2. Equivalent quantities can be defined for p-polarized light. With this approach, it is possible to show that:

$$\frac{\partial r_s}{\partial\varepsilon_1} = \frac{-\cos(\theta_{in})}{\sqrt{\tilde{n}^2 - \sin(\theta_{in})^2}}\frac{1}{\left[\cos(\theta_{in}) + \sqrt{\tilde{n}^2 - \sin(\theta_{in})^2}\right]^2}. \quad (19)$$

Furthermore, due to the fact that $\tilde{n}^2 = \varepsilon$,

$$\frac{\partial r_s}{\partial\varepsilon_1} = -i\frac{\partial r_s}{\partial\varepsilon_2} = \frac{1}{2\tilde{n}}\frac{\partial r_s}{\partial n} = \frac{-i}{2\tilde{n}}\frac{\partial r_s}{\partial k}, \quad (20)$$

which allows to compute the four sensitivities starting from Eq. (19).

Figure 19 reports, as an example, the sensitivity functions $S_n^{(R)}$, $S_k^{(R)}$, $S_{\varepsilon_1}^{(R)}$, and $S_{\varepsilon_2}^{(R)}$ calculated for Ge as a function of XUV photon energy and incidence angle[84]. The first thing to observe is that $S_n^{(R)}$ and $S_{\varepsilon_1}^{(R)}$ are one
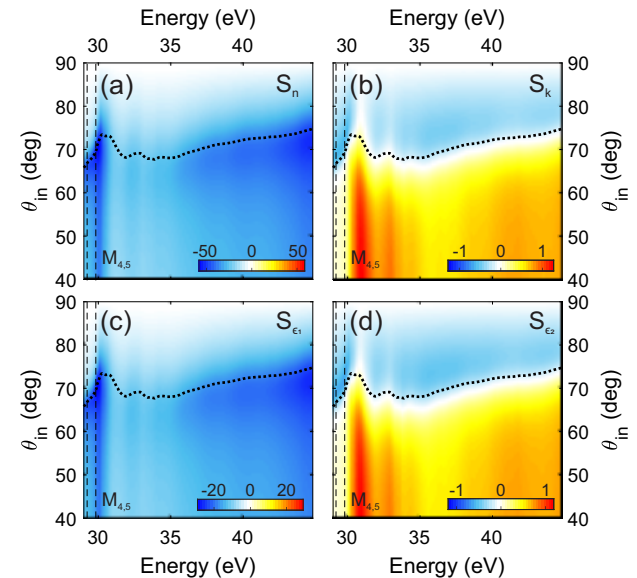

FIG. 19. Sensitivity functions $S_n^{(R)}$, **(a)**, $S_k^{(R)}$, **(b)**, $S_{\varepsilon_1}^{(R)}$, **(c)**, and $S_{\varepsilon_2}^{(R)}$, **(d)**, calculated starting from the Ge complex refractive index reported in[84], as a function of photon energy and angle of incidence. The critical angle for total external reflection (black dotted curve) follows a region of local minimum for $S_k^{(R)}$ and $S_{\varepsilon_2}^{(R)}$, while indicating the onset of large values of $S_n^{(R)}$ and $S_{\varepsilon_1}^{(R)}$.

order of magnitude larger than $S_k^{(R)}$ and $S_{\varepsilon_2}^{(R)}$. Following Eq. (19), this indicates that reflectivity measurements are generally more sensitive to the real part of $\tilde{n}$ and ε. It is worth noticing that, at the critical angle for total external reflection, $\theta_c = \arcsin(n_2/n_1)$ (black dotted curves in Fig. 19), $S_k^{(R)}$ and $S_{\varepsilon_2}^{(R)}$ approach zero, while $S_n^{(R)}$ and $S_{\varepsilon_1}^{(R)}$ are close to their maximum. Measurements performed at θ_c are therefore mostly insensitive to variations of the imaginary parts of $\tilde{n}$ and ε, helping their interpretation. This often makes θ_c the angle of choice to perform ATRS.

As discussed in Sec. III, ΔAbs is mainly related to the imaginary part of the refractive index (and of the material dielectric function, Fig. 16). As a consequence, transient absorption features can be directly mapped to vertical electronic transitions. Even at θ_c, the non-linear dependence of $\Delta R/R$ on $\tilde{n}$ (and ε) is responsible for the fact that resonant transitions do not give sharp features. Thus, the value of $\Delta R/R$ at a fixed energy value may depend on electronic excitations which lie far away in energy. Nevertheless, if both R' and R_0 are known on a reasonably wide energy axis, KK relations can be applied also to time-resolved measurements, as discussed for the

case of the static reflectivity. In such a case, reflectivity data can be translated in absorption properties, simplifying the interpretation (see Ref.[85]). To achieve instead a complete knowledge of the full, time-dependent complex dielectric function of the sample, alternative approaches must be devised (see Sec. V B).

B. Strengths and limitations

While it is clear that the need to control and change the light incidence angle makes the experimental setup for transient reflectivity more complex, ATRS certainly relaxes all the limitations related to the sample thickness. In fact, it allows investigating both bulk solids and thin layers deposited on substrates. Nevertheless, it is worth noticing that reflectivity measurements require a higher surface quality with respect to transmission-based techniques. If the sample surface roughness is too high, the incoming light is mostly scattered rather than reflected, and ATRS cannot be performed. Furthermore, the surface sensitivity of the technique makes it more susceptible to contamination or oxidation. To avoid possible severe artifacts, samples may require in situ preparation under ultra-high vacuum (UHV, $\sim 10^{-9}$ mbar) as done in photoemission experiments. The bulk sensitivity of ATAS makes this technique generally more forgiving than ATRS in terms of sample surface quality, allowing for ex-situ preparation and low high-vacuum (HV, $\sim 10^{-6}$ mbar) working conditions. Nevertheless, the optimal sample preparation procedure and vacuum level strongly vary with the sample thickness, its surface chemical reactivity, and the physics under scrutiny (see for example the effect of surface oxidation in the ATAS measurements performed in Ref.[81]). Therefore, depending on the target, ultra-high vacuum standards and complex sample preparation procedures may be needed.

Despite not all materials can be manufactured with optical-quality surfaces, the surface sensitivity of ATRS does not constitute only a technical limitation. As discussed in the previous section, the current detection systems make ATAS not suitable for the study of nanometric samples. Instead, the signal generated by the reflection from a very thin layer deposited on a substrate is measurable even for a thickness that approaches the single atomic layer. In Fig. 20(a), we report the simulated reflectivity of a WSe$_2$ sample of variable thickness, deposited on a SiO$_2$ substrate. The angle of incidence is chosen to be 75° with respect to normal incidence, while the XUV light is s-polarized. The energy region plotted covers the N$_{6,7}$ and O$_{2,3}$ edges of W (violet and brown dash-dotted lines, respectively) and the M$_{4,5}$ edges of Se (gray dash-dotted lines)[113]. As expected, the electronic transitions do not translate into sharp edges as in the absorption spectra (Fig. 20(b)), but rather in extended modulations of the reflectivity. Remarkably, these features are visible down to the monolayer case (0.5 nm, red curve in Fig. 20(a)), up to a 10% relative change
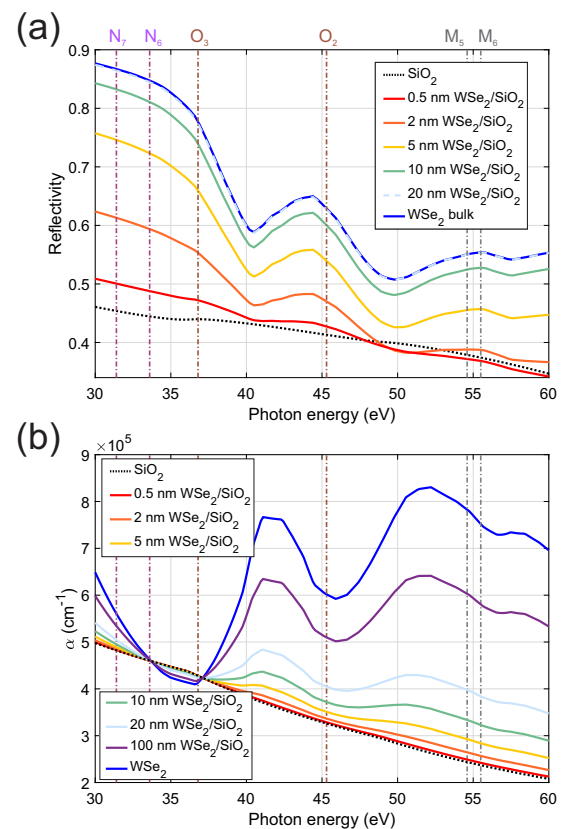

FIG. 20. **(a)** Simulated reflectivity for thin WSe$_2$ layers of diverse thickness, deposited on a SiO$_2$ bulk substrate. The light is s-polarized and $\theta_{in} = 75°$. The reported photon energy region covers the N$_{6,7}$ and O$_{2,3}$ edges of W (violet and brown dash-dotted lines, respectively) and the M$_{4,5}$ edges of Se (gray dash-dotted lines)[113]. **(b)** Average absorption of a WSe$_2$ layer of variable thickness, deposited onto a 50-nm SiO$_2$ substrate. Reflectivity and absorption data for both materials are taken from Henke database[125].

compared to the substrate, enabling their detection with current ATRS setups. Moreover, it is important to stress that the optical response of bulk WSe$_2$ (blue curve in Fig. 20(a)) coincides with the one of the 20-nm thick sample (dashed ciano curve in Fig. 20(a)) — a direct consequence of small penetration depth of XUV light in this material at 75° (around 5 nm, as found in Ref.[112]). The same does not hold for the absorption properties. The average absorption of a 0.5-nm WSe$_2$ layer deposited onto a relatively thin (50-nm) SiO$_2$ substrate (red curve in Fig. 20(b)), is almost identical to the one of the bare SiO$_2$ substrate (black dotted curve in Fig. 20(b)), with relative changes below 2%. While a detailed description of the optical properties of 2D materials goes beyond the scope of this work, it is important to stress that the way absorption and reflectivity are modelled at the monolayer limit may change from what reported in Sec. III and Sec. IV[126].

The possibility to work with samples of arbitrary thick-

nesses constitutes one of the main advantages of ATRS. The fabrication process of bulk crystals is in general more reliable and robust with respect to the realization of very thin layers, affecting the light-induced physical processes on ultrafast time scales[74]. For example, while high-quality bulk diamond crystals are commercially available, thin samples can be easily found only in a polycrystalline form, hindering a study of the effect of the crystal orientation. It is always possible to start from a bulk material and mechanically reduce its thickness (e.g. by ion beam milling), but this route can be extremely expensive and time-consuming when dealing with hard materials (e.g. diamond). In addition, the crystalline quality may be reduced during the process. Lastly, any thermal effect produced by the interaction with an intense pump pulse is better mitigated in bulk samples (or thin samples that are deposited on a thick substrate with good heat conduction), as in the case of Ge investigated in absorption[73] or reflection geometry[13,83]. In case of weak pumping, an efficient heat dissipation allows increasing the repetition rate, thus potentially reducing the measurement noise (see Secs. V A and V C).

One of the advantages of ATAS discussed in Sec. III B is the direct relationship between the absorption spectrum of a material and its unoccupied density of states, mapping the momentum-integrated band structure for all the electronic transitions satisfying the selection rules. For ATRS, instead, the Fresnel coefficient in Eq. (13) defines the complex link between the reflectance spectrum and the optical response of the material. As discussed before, the non-linear relation between R and $\tilde{n}$ prevents a direct assignment of spectral features in a reflectance spectrum to specific areas of the band structure. The same holds for transient reflectivity data, whose less direct interpretation constitutes the major limitation of the technique. Unfortunately, time-resolved multi-angle measurements are extremely costly from an experimental point of view. Therefore, this approach cannot be easily implemented with ATRS measurements. The second approach we discussed, based on KK analysis, is also hard to implement with pump-probe data, as it requires a priori information on the transient response of the material over a broad energy range (usually larger then what experimentally measured). In the visible range, variational approaches have been implemented to overcome this limitation[117,127]. However, their extension to the XUV range is not straightforward. These methods are based on the sensitivity of the measured spectra on n and k. If the measurements are performed at the critical angle θ_c, $S_k^{(R)}$ goes to zero and the variational approach cannot be applied. An incidence angle smaller than θ_c may give enough sensitivity (Fig. 19), at the cost of a lower $\Delta R/R$ detected. Thus, further technical developments are required to reach full knowledge of the time-dependent optical constants (see Sec. V B).

Lastly, for those materials where pump and probe pulses experience a substantially different $\tilde{n}$, the surface sensitivity of reflection-based spectroscopy may seriously challenge our description of the vacuum-solid interface. While in absorption one can account for the walk-off between the two beams by coupling the single-cell response with Maxwell equations while treating the sample surface as infinitesimally thin, the situation for the case of reflection is more complex. Remarkable examples are those materials that are transparent to the pump at the critical angle for the probe. In this case, indeed, the probe forms an evanescent wave in the solid that does not propagate in the direction perpendicular to the sample surface, while the pump does. The associated macroscopic system response may thus be impossible to directly compare with single-cell calculations, asking for more complete and time-consuming modeling of light-matter interaction at the interface. Depending on the complexity of the system and the number of edges involved, this may challenge the accurate interpretation of the attosecond timing of the system response with ATRS. Nevertheless, we believe that this current limitation is rather to be seen as a possible opportunity to investigate light-matter interaction on nanometric and attosecond scales, going beyond our macroscopic description of a solid.

V. CHALLENGES AND FUTURE DIRECTIONS

Despite the increasing interest in all-optical spectroscopic techniques, their extension to attosecond light sources so far did not show the same performances reached in the visible range, where signals of the order of $\Delta \text{OD} \sim 10^{-5} - 10^{-6}$ can be routinely detected. In this section, we discuss some of the present challenges to be faced, the possible workarounds so far devised, and some directions to be explored in the future.

A. Experimental noise suppression

The HHG process is highly nonlinear. For this reason, any instability in the generating field is enhanced in the XUV attosecond radiation. As an example, any intensity fluctuation of the driving radiation can determine both an energy shift and an intensity change in the XUV spectrum[128]. Due to the diverse generation schemes adopted, it is not easy to find a unique relation to translate the driving field instabilities into measurement noise. Nevertheless, one can fairly state that discrete harmonics are less affected by energy fluctuations of the driving laser than single attosecond pulses, as these latter require more complex generation schemes, that may introduce other sources of instability[129]. Furthermore, single attosecond pulse generation is also usually sensitive to the carrier-envelope phase (CEP) of the driving pulses, in a fashion that depends on the specific gating scheme employed. Any CEP fluctuation can lead on its own to significant changes in the spectral amplitude of the attosecond radiation, ultimately introducing severe modulations if the CEP is so unstable to cause the gen-

eration of multiple attosecond pulses. These changes in the XUV spectral power are detrimental to all-optical measurements, since any unwanted variation results in measurement artifacts (noise).

To minimize the noise contribution coming from spectral fluctuations, the customary solution in both ATAS and ATRS is to implement referencing techniques[128]. As introduced in Sec. III, a mechanical shutter (or chopper) blocks the pump beam periodically, allowing the acquisition of reference pump-off spectra. This periodic modulation of the pump signal allows to reject noise contributions with a characteristic frequency smaller than the inverse of the chopping period. Therefore, to maximize noise rejection, large chopping frequencies are beneficial. The ultimate frequency limit of this approach is half the repetition rate of the laser source, i.e. at least one laser shot per shutter status must be acquired. However, in typical ATAS and ATRS experiments, this limit cannot be reached. First, the flux of HHG sources is usually low compared to what can be obtained in other spectral regions (HHG conversion efficiency is typically below 10^{-5}–10^{-6}), and it is further decreased by the interaction with the sample, whose transmission or reflection coefficient is typically small. Thus, to fully exploit the dynamical range of the detector, integration over multiple laser shots is required, decreasing the chopping rate. In addition, even if the source flux were high enough, a hard boundary is represented by the readout time of detectors. Typical readout times are about $20\,\mathrm{ms}$, thus limiting the maximum chopping frequency to $25\,\mathrm{Hz}$, unless either the spectral span or the signal-to-noise ratio is sacrificed. This made it so far impossible to apply lock-in detection and boxcar integration, which are instead fundamental for spectrally-integrated acquisition schemes[130]. The combined effect of the poor stability and low efficiency of HHG sources, together with the slow readout time of detectors, makes it quite challenging to detect signals with $\Delta\mathrm{OD} < 10^{-3}$, while $\Delta\mathrm{OD} \lesssim 10^{-5}$ can be reached by transient absorption measurements in the optical spectral region[131,132].

Since the amplitude of transient features typically depends on the pump intensity, the limited sensitivity of ATAS and ATRS forces the employment of high pump fluences, approaching the damage threshold of the investigated sample. So far, this limited most of the ATAS and ATRS experiments to the strong-field regime[69,92,104,105], hindered the investigation of thin layers, and made thermal load management in ATAS critical[73]. Moreover, it made the study of low-excitation regimes, such as those involved in photovoltaics, or in electronic and structural phase transitions[133], a hard task, thus limiting the application range of these techniques.

To overcome these limitations, several noise suppression methods were devised. They can be divided into two classes: the first relies on more complex detection systems, while the second focuses on post-processing analyses. For the former category, the core idea is to acquire a simultaneous reference signal (e.g. the spectrum of the
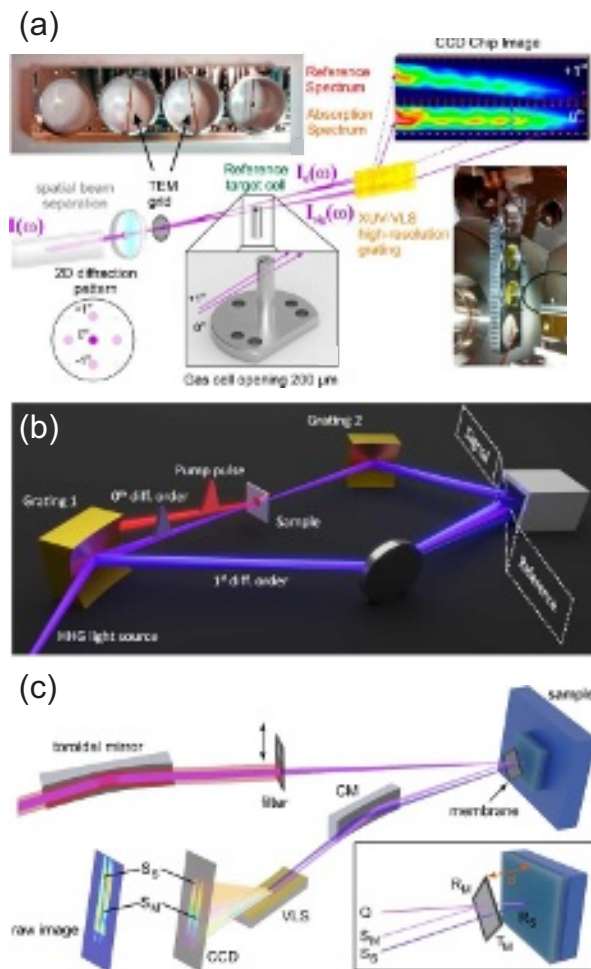

FIG. 21. Experimental setups for noise reduction. **(a)** A properly designed copper-mesh TEM grid diffracts the XUV probe beam. The zeroth diffraction order interacts with the sample, while one of the first order diffraction beams is detected as a reference. Reproduced from[134], with the permission of AIP Publishing. **(b)** The specular reflection of a diffraction grating interacts with the pumped sample, and is subsequently analyzed by an XUV spectrometer. The first diffraction order, instead, is steered to the same CCD camera by grazing incidence optics, serving as a reference beam. Reproduced from[135]. CC BY 4.0. **(c)** A thin Si_3N_4 membrane in close proximity of the sample acts as an XUV beam splitter. The reflected radiation gives the reference beam, while the transmitted portion interacts with the sample and is then transmitted by the membrane. Reproduced from[136]. CC BY 4.0.

incoming radiation) to be able to distinguish between pump-induced variations and spectral fluctuations of the laser source. This approach, which is straightforward in the visible and near-infrared spectral regions[131,132] where beam splitters are commercially available, can be extended to the XUV spectrum. For absorption measurements, one possible implementation consists of diffracting a portion of the beam with a properly designed copper-

mesh grid for transmission electron microscopy (TEM)[134] (Fig. 21(a)). After the diffractive optical element, only the zeroth-order beam interacts with the sample. Then, both the zeroth- and first-order beams impinge on the same grazing-incidence diffraction grating and are acquired by the same charge-coupled device camera. By properly calibrating the acquisition scheme, accounting for the non-uniform diffraction efficiency of the grid, and for possible spatial inhomogeneities in the detector, a direct referencing of the measured XUV spectrum is obtained[134]. Another possibility is to use, as a diffractive optical element, a plane grazing-incidence diffraction grating for XUV radiation[137]. Also in this case, the zeroth-order specular reflection is used as a probe beam, while the first-order diffracted beam can be either directly imaged by a dedicated detector[137] or steered with grazing-incidence mirrors to the same camera[135] (Fig. 21(b)). In both cases, direct referencing is achieved after accounting either for differences in the two detectors or for the reflectivity of additional grazing-incidence optical elements. In a reflectivity geometry, instead, precise and absolute measurements have been obtained by placing a thin Si_3N_4 membrane in close proximity (within the Rayleigh range of the XUV focus) and parallel to the surface to be probed[136] (Fig. 21(c)). The thin membrane acts as a beam splitter for XUV radiation: the transmitted portion impinges on the sample surface and is transmitted again by the membrane, while the specular reflection of the membrane gives the reference beam. Despite being technically challenging, this method proved a sensitivity almost comparable with that achieved at synchrotron radiation facilities, and its extension to pump-probe measurements is envisioned[136]. These schemes, which have already been exploited to measure ultrafast magnetization[138] and coupled electronic and structural[133] dynamics, in principle allow directly measuring the shot-to-shot spectral fluctuations. However, this comes with a considerable increase in the complexity of the experimental setup and a further reduction of the XUV photon flux.

Tackling the same problem from a different perspective, post-processing noise reduction methods can help decreasing the noise level. The main observation, in this case, is that the noise contribution in the optical density can be mainly written as a multiplicative noise factor and an additive noise term[139]. As the former is typically much smaller than the signal to be measured, thus being negligible, noise reduction algorithms focus on the additive contribution, related to XUV spectral variations. Since fluctuations in the HHG spectra are strongly correlated to the parameters of the driving field as the input laser energy, monitoring its changes with a photodiode allows partially compensating their effect[128]. In particular, Volkov et al. demonstrated the intensity-dependent non-adiabatic blueshift of the driving field in the gas cell to be the dominant noise contribution in XUV spectra[128]. An alternative approach is to take advantage of the strong correlations between different wavelengths in the XUV

radiation. This allows to relate the noise contributions in a certain spectral range to fluctuations in a different one by the so-called correlation matrix between different pixels of the detector. Typically, it can be determined by measuring pump-off spectra in close sequence (also called calibration dataset) as in this configuration any residual signal in the optical density map comes from noise. A possible method, dubbed edge-pixel referencing[139], is based on the assumption that there exists an energy range with non-negligible spectral intensity but without any pump-induced signal, called the edge-pixel region. In this case, starting from the calibration dataset, one can compute the correlation matrix, which relates noise contributions in the edge-pixel region to fluctuations in any other energy range, enabling efficient noise removal from the measurement itself. This method led to a five-fold reduction of correlated noise and already proved to be applicable to standard ATAS[139] and ATRS[13,66] schemes without any additional modification. The main drawback of the edge-pixel referencing method is that it requires a region free from pump-induced features, otherwise artifacts will be mapped at different energies by the correlation matrix. The adaptive iteratively reweighted principal component regression method[140] (airPCR) solves this issue. The method is based on the identification of a limited set of linearly independent principal components that describe the calibration dataset and thus the correlated noise. The noise contribution to the pump-probe measurement can then be determined by performing a fit based on the components. A re-weighting algorithm allows iteratively evaluating whether each pixel is free from pump-induced features or not, changing the pixel interval on which principal components are fitted and reducing the risk for creating of artifacts. The main challenge in airPCR is to find an optimal exit condition for the iterative algorithm. This method allows reaching $\Delta OD < 10^{-3}$ without any prior assumption on the energy span of the pump-induced features[140], which in the case of ATAS and ATRS can easily reach several tens of eV.

In conclusion, despite the intense, recent effort both on the hardware[134,135,137] and software[128,139,140] side, the instability of HHG sources is currently the major issue for ATAS and ATRS. Further improvements in experimental noise suppression are needed to reach the sensitivity already achieved in other spectral regions and allow the investigation of subtler phenomena and weaker excitation regimes.

B. Interferometric approaches

As discussed in Secs. III and IV, absorption measurements are mainly sensitive to the imaginary part of ε, while reflectivity is determined by both its real and imaginary components, depending on the incidence angle. In principle, full information on the equilibrium and transient optical properties of the investigated sample can be

obtained through the KK relations[141], as done for equilibrium reflectivity measurements performed with synchrotron radiation[86,142]. They require computing an integral over an infinite photon frequency range (see Eq. (15)), usually not known. Nevertheless, they can be applied to measurements performed over a limited domain by truncating the integral (thus obtaining approximated solutions), padding with data from the literature and extrapolating over unknown frequencies. This method has already been successfully employed to discuss the equilibrium optical properties measured by HHG-based sources[13,85]. Its extension to ATAS and ATRS measurements is less straightforward. A crucial hypothesis, in fact, is the causality principle[141], whose validity can be questionable in the case of attosecond light pulses[143]. For instance, the transmittance of an XUV attosecond pulse through a medium can be modified by a pumping pulse even outside their temporal overlap. Free induction decay is a notable example: a pump pulse can disturb the emission of XUV radiation after coherent excitation even long after the XUV pulse has interacted with the sample[144]. It is important to notice that this does not imply any global causality violation since the lifetime of excited states must be accounted for. Nevertheless, the validity of the causality principle has to be carefully considered depending on the exact experimental conditions[143].

In the visible and IR spectral regions, KK relations have already allowed extracting quantitative information from transient absorption and reflectivity experiments with femtosecond temporal resolution[117]. By exploiting the linearity of these equations, the transient optical properties of the sample can be modeled as the weighted sum of KK-consistent functions, where the weights are determined by a variational fitting procedure[127,145]. This method has never been applied to ATAS and ATRS measurements, which are challenging because of their broad spectral coverage, the possible presence of stronger features outside the XUV range[117], and the angle-dependent sensitivity in ATRS measurements. So far, full information on the optical constants with KK relations was obtained only by fitting measurements with phenomenological models of the investigated physical system[66,83] or exploiting the energy localization of core-excitonic features to reduce the integration domain[85].

A different approach is based on interferometric techniques capable of assessing both the amplitude and phase of the optical response (such as the Fresnel reflection or absorption coefficients) instead of their squared modulus (reflectance/transmittance). Since in the XUV spectral region efficient beam splitters are not available, the first scheme to be demonstrated was based on Young double slit geometry. A 0–π square-wave phase grating placed in the IR path prior to HHG, creates two focal spots in the generating medium, thus giving two spatially-separated HHG sources which can be refocused onto the solid target[146]. In the far field (e.g., in the detector plane), the radiation from the two sources interferes, generating an additional periodic modulation of the XUV spectrum in the non-dispersive direction of the XUV spectrometer. With this scheme it is possible to overlap the IR pump to only one XUV spot on target and unbalance the interferometer. Variations in the full electric susceptibility can be then retrieved by tracking the relative changes in the amplitude and phase of the interference pattern in the XUV spectrum[143].

This interferometric approach has already been employed to retrieve the full complex optical response of atomic and molecular targets[143,147–152] or to characterize light beams[153]. However, a direct application to solid-state samples is, to the best of our knowledge, still missing. Interferometric techniques would allow measuring pump-induced variations in the full complex and time-dependent dielectric constant of samples. As an example, this could enable a direct retrieval of the characteristics of core excitons[79,85,87] without the need for iterative algorithms[90], or fully determining the electric polarization, which relates to the electric field and the complex susceptibility, to study the reversible and irreversible energy transfer between the sample and the field[154].

C. Photon energy and repetition rate

The future capabilities of ATAS and ATRS measurements are obviously strongly linked with advancements in HHG sources. Until the last decade, Ti:sapphire lasers represented the customary choice in attosecond science[155]. More recently, the development of mid-IR optical parametric amplifiers and of industrial-grade fiber lasers enriched the possibilities, allowing extending the range of HHG-based sources to the soft X-ray and increasing their repetition rate[156,157]. This will certainly impact ATAS and ATRS measurements, increasing the number of reachable absorption edges, making the interpretation of experimental data easier, reducing measurement times, and allowing increasing their signal-to-noise ratio.

According to a semiclassical description of HHG[158–160], the cut-off photon energy, $\hbar\omega_{max} = I_p + 3.17U_p$, depends on the ionization potential of the gas target, I_p, and on the ponderomotive energy of an electron oscillating in the driving field, U_p. As the latter scales quadratically with the driving wavelength, the employment of mid-IR lasers as generating fields can lead to soft X-ray generation with HHG setups[161]. Unfortunately, the cut-off extension comes at the expense of the HHG flux, since the conversion efficiency scales as λ^{-5}–λ^{-7}.

Li and coworkers first reached a spectral coverage up to the carbon K-absorption edge (284 eV) by focusing a two-cycle 1.8-μm driver into a He target, and characterized the radiation with the attosecond streaking technique[162]. Isolated pulses, obtained by gating the emission process with the polarization gating technique[163], were characterized by the phase retrieval by omega oscillation filtering (PROOF)[164]. In the same year, Gaum-

nitz et al. reported the generation of spectra extending up to 190 eV in Ne without exploiting any gating technique[165]. Also in this case, an attosecond streaking measurement allowed demonstrating the emission of an isolated soft X-ray pulse, which was characterized with the multi-line Volkov-transform generalized projection algorithm[165]. Cousin and coworkers further extended the cutoff energy of single attosecond pulses to 350 eV[166]. These energies are significantly within the transparency window of water in the soft X-ray region, between the K-absorption edges of carbon (282 eV) and of oxygen (533 eV). For high-quality driving beams, increasing the driving intensity way beyond its critical value, further extends the cutoff, up to more than 550 eV in He[167]. The same scheme could be exploited for shorter wavelength drivers[168], while achieving control over the driving field via parametric waveform synthesis could also be beneficial[169].

The first, obvious advantage of extending the cutoff of the HHG process is the possibility of covering several new absorption edges compared to those available in the XUV spectral region[106] (Fig. 22). This not only allows probing simultaneously different edges, which helps decoupling charge, spin, and lattice dynamics of the different elemental components[114,119], but also enables the ionization of more tightly bound core states. K- and L-edges (Fig. 22), are typically sharper than M ones and associated with stronger, element-specific features, substantially helping the physical interpretation of the experimental data. For example, recent works have shown the possibility to access the unoccupied density of electronic states with K-edge ATAS[115] or to study the influence of the electronic band structure on carrier dynamics, especially when these are excited in the proximity of a Van Hove singularity[171]. In the future, the development of novel and more robust laser sources with longer central wavelength, as Yb- and Tm-based sources, will allow increasing the generation efficiency, and to explore alternative generation schemes.

Yb-based sources hold the promise for further increasing the repetition rate, even up to a 1 MHz and more[172,173]. Both in the soft X-ray and XUV spectral region, upscaling the repetition rate allows increasing the spectral brightness of the source[174], i.e. the number of photons per second in a given spectral region. This reduces the integration time that is needed to obtain a detectable signal and, in turn, the noise. This possibility is fascinating since it could allow reducing the pump fluence and start investigating ultrafast dynamics in lower charge injection regimes[135]. However, too large repetition rates could also induce thermal effects[73] or damage the solid sample, thus being incompatible with fragile or thin samples, especially for ATAS.

In conclusion, ATAS and ATRS will strongly benefit from developments both in laser technology and in novel HHG schemes. The latter, in particular, will allow routinely entering the soft X-ray spectral region, where many more absorption edges are available and

the interpretation of experimental measurements is easier. The generation of isolated attosecond pulses reaching the K-absorption edge of carbon (282 eV) will be fundamental for studying novel organic materials[161,175], which hold promises for optoelectronic applications. Further increasing the cutoff energy up to the K-absorption edge of oxygen (533 eV), in turn, will help addressing many fundamental questions in condensed matter physics, for instance allowing the investigation of transition metal oxides[124,176] on the attosecond time scale.

VI. CONCLUSIONS

In this perspective article, we have reviewed the extension of transient absorption and reflection spectroscopy to the attosecond domain and solid samples. Starting from a historical overview, we have shown how these techniques offer the possibility to perform all-optical spectroscopy, with particular attention to the ultrafast electron dynamics that unfold during light-matter interaction, before any intra- or inter-valley relaxation can occur. After having introduced the principle of both techniques, presenting both their strengths and weaknesses, we have then discussed the current challenges and possible future directions that may allow us to overcome them.

While the first pioneering experiments have already proved the capabilities of ATAS and ATRS, further development is needed to reach the sensitivity of a few parts per million, typical of these techniques in the visible and IR spectral ranges. Pushed by the recent progress in unconventional sources of high-order harmonics and fast XUV detectors, we foresee that ATAS and ATRS will establish among the main tools capable of giving us a deep understanding of the interplay between ultrafast resonant and non-resonant processes triggered by light in matter, fundamental to designing optoelectronic devices with an optimized, efficient carrier injection rate and minimized required optical power. By unveiling elusive phenomena in physical systems with concrete impact in high-tech applications (electronics, photovoltaics, and photonics), these attosecond all-optical spectroscopies will foster our knowledge of fundamental mechanisms related to charge excitation and control, which may soon find application to more efficient transfer of energy and information, with a profound impact on technology and society.
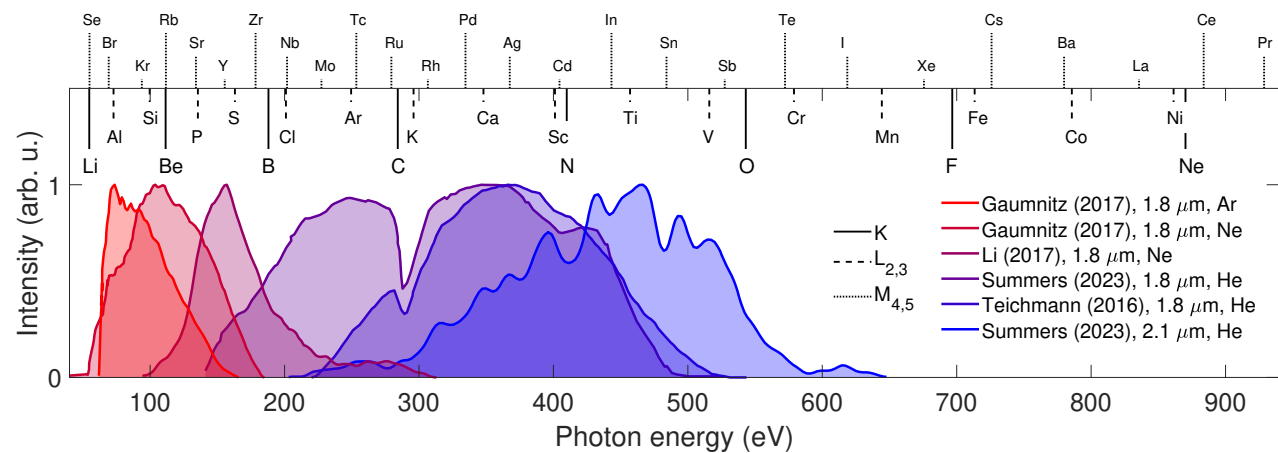
ACKNOWLEDGMENTS

FIG. 22. Soft X-ray spectra generated by HHG in different conditions[115,162,165,170] (colored curves). By changing the driving wavelength (1.8 and 2.1 μm) and the gas target (Ar, Ne, He), the radiation can range from 50 to 650 eV, covering the K (black solid lines), $L_{2,3}$ (black dashed lines) and $M_{4,5}$ (black dotted lines) electron binding energies of several elements[125]. Reproduced from[115,162,165,170].

DATA AVAILABILITY STATEMENT

Data sharing not applicable – no new data generated.

REFERENCES

[1]R. Borrego-Varillas, M. Lucchini, and M. Nisoli, Reports on Progress in Physics **85**, 066401 (2022).

[2]D. Hui, H. Alqattan, S. Yamada, V. Pervak, K. Yabana, and M. T. Hassan, Nature Photonics **16**, 33 (2022).

[3]A. Schiffrin, T. Paasch-Colberg, N. Karpowicz, V. Apalkov, D. Gerster, S. Mühlbrandt, M. Korbman, J. Reichert, M. Schultze, S. Holzner, J. V. Barth, R. Kienberger, R. Ernstorfer, V. S. Yakovlev, M. I. Stockman, and F. Krausz, Nature **493**, 70 (2013).

[4]T. Paasch-Colberg, S. Y. Kruchinin, Özge Sağlam, S. Kapser, S. Cabrini, S. Muehlbrandt, J. Reichert, J. V. Barth, R. Ernstorfer, R. Kienberger, V. S. Yakovlev, N. Karpowicz, and A. Schiffrin, Optica **3**, 1358 (2016).

[5]F. Siegrist, J. A. Gessner, M. Ossiander, C. Denker, Y.-P. Chang, M. C. Schröder, A. Guggenmos, Y. Cui, J. Walowski, U. Martens, J. K. Dewhurst, U. Kleineberg, M. Münzenberg, S. Sharma, and M. Schultze, Nature **571**, 240 (2019).

[6]T. Higuchi, C. Heide, K. Ullmann, H. B. Weber, and P. Hommelhoff, Nature **550**, 224 (2017).

[7]T. Paasch-Colberg, A. Schiffrin, N. Karpowicz, S. Kruchinin, Özge Sağlam, S. Keiber, O. Razskazovskaya, S. Mühlbrandt, A. Alnaser, M. Kübel, V. Apalkov, D. Gerster, J. Reichert, T. Wittmann, J. V. Barth, M. I. Stockman, R. Ernstorfer, V. S. Yakovlev, R. Kienberger, and F. Krausz, Nature Photonics **8**, 214 (2014).

[8]I. Pupeza, M. Huber, M. Trubetskov, W. Schweinberger, S. A. Hussain, C. Hofer, K. Fritsch, M. Poetzlberger, L. Vamos, E. Fill, T. Amotchkina, K. V. Kepesidis, A. Apolonski, N. Karpowicz, V. Pervak, O. Pronin, F. Fleischmann, A. Azzeer, M. Žigman, and F. Krausz, Nature **577**, 52 (2020).

[9]H. J. Caulfield and S. Dolev, Nature Photonics **4**, 261 (2010).

[10]T. Boolakee, C. Heide, A. Garzón-Ramírez, H. B. Weber, I. Franco, and P. Hommelhoff, Nature **605**, 251 (2022).

[11]C. R. McDonald, G. Vampa, P. B. Corkum, and T. Brabec, Physical Review Letters **118**, 173601 (2017).

[12]M. Ossiander, K. Golyari, K. Scharl, L. Lehnert, F. Siegrist, J. P. Bürger, D. Zimin, J. A. Gessner, M. Weidman, I. Floss, V. Smejkal, S. Donsa, C. Lemell, F. Libisch, N. Karpowicz, J. Burgdörfer, F. Krausz, and M. Schultze, Nature Communications **13**, 1620 (2022).

[13]G. Inzani, L. Adamska, A. Eskandari-asl, N. D. Palo, G. L. Dolso, B. Moio, L. J. D'Onofrio, A. Lamperti, A. Molle, R. Borrego-Varillas, M. Nisoli, S. Pittalis, C. A. Rozzi, A. Avella, and M. Lucchini, Nature Photonics **17**, 1059 (2023).

[14]S. Ghimire, A. D. DiChiara, E. Sistrunk, P. Agostini, L. F. DiMauro, and D. A. Reis, Nature Physics **7**, 138 (2011).

[15]G. Vampa, C. McDonald, G. Orlando, D. Klug, P. Corkum, and T. Brabec, Physical Review Letters **113**, 073901 (2014).

[16]T. T. Luu, M. Garg, S. Y. Kruchinin, A. Moulet, M. T. Hassan, and E. Goulielmakis, Nature **521**, 498 (2015).

[17]A. J. Uzan, G. Orenstein, Álvaro Jiménez-Galán, C. McDonald, R. E. F. Silva, B. D. Bruner, N. D. Klimkin, V. Blanchet, T. Arusi-Parpar, M. Krüger, A. N. Rubtsov, O. Smirnova, M. Ivanov, B. Yan, T. Brabec, and N. Dudovich, Nature Photonics **14**, 183 (2020).

[18]P. Jürgens, B. Liewehr, B. Kruse, C. Peltz, D. Engel, A. Husakou, T. Witting, M. Ivanov, M. J. J. Vrakking, T. Fennel, and A. Mermillod-Blondin, Nature Physics **16**, 1035 (2020).

[19]J. D. Gaynor, A. P. Fidler, Y.-C. Lin, H.-T. Chang, M. Zuerch, D. M. Neumark, and S. R. Leone, Physical Review B **103**, 245140 (2021).

[20]S. Ghimire and D. A. Reis, Nature Physics **15**, 10 (2019).

[21]E. Goulielmakis and T. Brabec, Nature Photonics **16**, 411 (2022).

[22]S. R. Leone and D. M. Neumark, Science **379**, 536 (2023).

[23]In the present article, we have tried to include all representative papers. Given the existence of a vast number of relevant literature in the field, we apologize for any unintentional omission of original research papers having significant contribution on the development of the field.

[24]G. Farkas and C. Tóth, Physics Letters A **168**, 447 (1992).

[25]P. Antoine, A. L'Huillier, and M. Lewenstein, Physical Review Letters **77**, 1234 (1996).

[26]M. B. Gaarde and K. J. Schafer, Phys. Rev. Lett. **89**, 213901 (2002).

[27] F. Krausz and M. Ivanov, Reviews of Modern Physics **81**, 163 (2009).

[28] M. Nisoli, P. Decleva, F. Calegari, A. Palacios, and F. Martín, Chemical Reviews **117**, 10760 (2017), pMID: 28488433.

[29] R. Borrego-Varillas and M. Lucchini, Opt. Express **29**, 9711 (2021).

[30] S. Hüfner, *Photoelectron Spectroscopy*, Advanced Texts in Physics (Springer Berlin Heidelberg, Berlin, Heidelberg, 2003).

[31] L. Kasmi, M. Lucchini, L. Castiglioni, P. Kliuiev, J. Osterwalder, M. Hengsberger, L. Gallmann, P. Krüger, and U. Keller, Optica **4**, 1492 (2017).

[32] J. Ullrich, R. Moshammer, A. Dorn, R. Dörner, L. P. H. Schmidt, and H. Schmidt-Böcking, Reports on Progress in Physics **66**, 1463 (2003).

[33] J. Vos, L. Cattaneo, S. Patchkovskii, T. Zimmermann, C. Cirelli, M. Lucchini, A. Kheifets, A. S. Landsman, and U. Keller, Science **360**, 1326 (2018).

[34] L. B. Madsen, American Journal of Physics **73**, 57 (2005).

[35] M. Lucchini, F. Medeghini, Y. Wu, F. Vismarra, R. Borrego-Varillas, A. Crego, F. Frassetto, L. Poletto, S. A. Sato, H. Hübener, U. D. Giovannini, Ángel Rubio, and M. Nisoli, Nature Communications **13**, 7103 (2022).

[36] L. Gallmann, J. Herrmann, R. Locher, M. Sabbar, A. Ludwig, M. Lucchini, and U. Keller, Molecular Physics **111**, 2243 (2013).

[37] R. Geneaux, H. J. B. Marroux, A. Guggenmos, D. M. Neumark, and S. R. Leone, Philosophical Transactions of the Royal Society A: Mathematical, Physical and Engineering Sciences **377**, 20170463 (2019).

[38] Z.-H. Loh, M. Khalil, R. E. Correa, R. Santra, C. Buth, and S. R. Leone, Phys. Rev. Lett. **98**, 143601 (2007).

[39] Z.-H. Loh, C. H. Greene, and S. R. Leone, Chemical Physics **350**, 7 (2008).

[40] E. Goulielmakis, Z.-H. Loh, A. Wirth, R. Santra, N. Rohringer, V. S. Yakovlev, S. Zherebtsov, T. Pfeifer, A. M. Azzeer, M. F. Kling, S. R. Leone, and F. Krausz, Nature **466**, 739 (2010).

[41] H. Wang, M. Chini, S. Chen, C.-H. Zhang, F. He, Y. Cheng, Y. Wu, U. Thumm, and Z. Chang, Phys. Rev. Lett. **105**, 143002 (2010).

[42] M. Holler, F. Schapper, L. Gallmann, and U. Keller, Phys. Rev. Lett. **106**, 123601 (2011).

[43] M. Lucchini, A. Ludwig, T. Zimmermann, L. Kasmi, J. Herrmann, A. Scrinzi, A. S. Landsman, L. Gallmann, and U. Keller, Physical Review A **91**, 063406 (2015).

[44] M. Chini, B. Zhao, H. Wang, Y. Cheng, S. X. Hu, and Z. Chang, Phys. Rev. Lett. **109**, 073601 (2012).

[45] C.-T. Liao, A. Sandhu, S. Camp, K. J. Schafer, and M. B. Gaarde, Phys. Rev. Lett. **114**, 143002 (2015).

[46] M. Chini, X. Wang, Y. Cheng, Y. Wu, D. Zhao, D. a. Telnov, S.-I. Chu, and Z. Chang, Scientific Reports **3**, 1105 (2013).

[47] M. Lucchini, J. Herrmann, A. Ludwig, R. Locher, M. Sabbar, L. Gallmann, and U. Keller, New Journal of Physics **15**, 103010 (2013).

[48] C. Ott, A. Kaldun, P. Raith, K. Meyer, M. Laux, J. Evers, C. H. Keitel, C. H. Greene, and T. Pfeifer, Science **340**, 716 (2013).

[49] C. Ott, A. Kaldun, L. Argenti, P. Raith, K. Meyer, M. Laux, Y. Zhang, A. Blättermann, S. Hagstotz, T. Ding, and et al., Nature **516**, 374 (2014).

[50] J. Herrmann, M. Lucchini, S. Chen, M. Wu, A. Ludwig, L. Kasmi, K. J. Schafer, L. Gallmann, M. B. Gaarde, and U. Keller, New Journal of Physics **17**, 013007 (2015).

[51] Y. Cheng, M. Chini, X. Wang, A. González-Castrillo, A. Palacios, L. Argenti, F. Martín, and Z. Chang, Phys. Rev. A **94**, 023403 (2016).

[52] M. Reduzzi, W.-C. Chu, C. Feng, A. Dubrouil, J. Hummert, F. Calegari, F. Frassetto, L. Poletto, O. Kornilov, M. Nisoli, C.-D. Lin, and G. Sansone, Journal of Physics B: Atomic, Molecular and Optical Physics **49**, 065102 (2016).

[53] E. R. Warrick, W. Cao, D. M. Neumark, and S. R. Leone, The Journal of Physical Chemistry A **120**, 3165 (2016).

[54] Y. Kobayashi, K. F. Chang, T. Zeng, D. M. Neumark, and S. R. Leone, Science **365**, 79 (2019).

[55] H. Timmers, X. Zhu, Z. Li, Y. Kobayashi, M. Sabbar, M. Hollstein, M. Reduzzi, T. J. Martínez, D. M. Neumark, and S. R. Leone, Nature Communications **10**, 3133 (2019).

[56] K. F. Chang, M. Reduzzi, H. Wang, S. Poullain, Y. Kobayashi, L. Barreau, D. Prendergast, D. M. Neumark, and S. R. Leone, Nature Communications **11**, 4042 (2020).

[57] K. S. Zinchenko, F. Ardana-Lamas, I. Seidu, S. P. Neville, J. van der Veen, V. U. Lanfaloni, M. S. Schuurman, and H. J. Wörner, Science **371**, 489 (2021).

[58] D. T. Matselyukh, V. Despré, N. V. Golubev, A. I. Kuleff, and H. J. Wörner, Nature Physics **18**, 1206 (2022).

[59] A. R. Attar, A. Bhattacherjee, C. D. Pemmaraju, K. Schnorr, K. D. Closser, D. Prendergast, and S. R. Leone, Science **356**, 54 (2017).

[60] Y. Pertot, C. Schmidt, M. Matthews, A. Chauvet, M. Huppert, V. Svoboda, A. von Conta, A. Tehlar, D. Baykusheva, J.-P. Wolf, and H. J. Wörner, Science **355**, 264 (2017).

[61] N. Saito, H. Sannohe, N. Ishii, T. Kanai, N. Kosugi, Y. Wu, A. Chew, S. Han, Z. Chang, and J. Itatani, Optica **6**, 1542 (2019).

[62] E. Ridente, D. Hait, E. A. Haugen, A. D. Ross, D. M. Neumark, M. Head-Gordon, and S. R. Leone, Science **380**, 713 (2023).

[63] M. Rebholz, T. Ding, V. Despré, L. Aufleger, M. Hartmann, K. Meyer, V. Stooß, A. Magunia, D. Wachs, P. Birk, Y. Mi, G. D. Borisova, C. d. C. Castanheira, P. Rupprecht, G. Schmid, K. Schnorr, C. D. Schröter, R. Moshammer, Z.-H. Loh, A. R. Attar, S. R. Leone, T. Gaumnitz, H. J. Wörner, S. Roling, M. Butz, H. Zacharias, S. Düsterer, R. Treusch, G. Brenner, J. Vester, A. I. Kuleff, C. Ott, and T. Pfeifer, Phys. Rev. X **11**, 031001 (2021).

[64] Z. Yin, Y.-P. Chang, T. Balčiūnas, Y. Shakya, A. Djorović, G. Gaulier, G. Fazio, R. Santra, L. Inhester, J.-P. Wolf, and H. J. Wörner, Nature (2023), 10.1038/s41586-023-06182-6.

[65] E. Papalazarou, D. Boschetto, J. Gautier, T. Garl, C. Valentin, G. Rey, P. Zeitoun, A. Rousse, P. Balcou, and M. Marsi, Applied Physics Letters **93**, 041114 (2008).

[66] R. Géneaux, I. Timrov, C. J. Kaplan, A. D. Ross, P. M. Kraus, and S. R. Leone, Phys. Rev. Res. **3**, 033210 (2021).

[67] C. La-O-Vorakiat, M. Siemens, M. M. Murnane, H. C. Kapteyn, S. Mathias, M. Aeschlimann, P. Grychtol, R. Adam, C. M. Schneider, J. M. Shaw, H. Nembach, and T. J. Silva, Phys. Rev. Lett. **103**, 257402 (2009).

[68] D. Rudolf, C. La-O-Vorakiat, M. Battiato, R. Adam, J. M. Shaw, E. Turgut, P. Maldonado, S. Mathias, P. Grychtol, H. T. Nembach, T. J. Silva, M. Aeschlimann, H. C. Kapteyn, M. M. Murnane, C. M. Schneider, and P. M. Oppeneer, Nature Communications **3**, 1037 (2012).

[69] M. Schultze, E. M. Bothschafter, A. Sommer, S. Holzner, W. Schweinberger, M. Fiess, M. Hofstetter, R. Kienberger, V. Apalkov, V. S. Yakovlev, M. I. Stockman, and F. Krausz, Nature **493**, 75 (2013).

[70] L. J. Borja, M. Zürch, C. D. Pemmaraju, M. Schultze, K. Ramasesha, A. Gandman, J. S. Prell, D. Prendergast, D. M. Neumark, and S. R. Leone, Journal of the Optical Society of America B **33**, C57 (2016).

[71] J. Vura-Weis, C.-M. Jiang, C. Liu, H. Gao, J. M. Lucas, F. M. F. de Groot, P. Yang, A. P. Alivisatos, and S. R. Leone, The Journal of Physical Chemistry Letters **4**, 3667 (2013).

[72] C.-M. Jiang, L. R. Baker, J. M. Lucas, J. Vura-Weis, A. P. Alivisatos, and S. R. Leone, The Journal of Physical Chemistry C **118**, 22774 (2014).

[73] M. Zürch, H.-t. Chang, L. J. Borja, P. M. Kraus, S. K. Cushing, A. Gandman, C. J. Kaplan, M. H. Oh, J. S. Prell, D. Prendergast, C. D. Pemmaraju, D. M. Neumark, and S. R. Leone, Nature Communications **8**, 15734 (2017).

[74] M. Zürch, H.-T. Chang, P. M. Kraus, S. K. Cushing, L. J. Borja, A. Gandman, C. J. Kaplan, M. H. Oh, J. S. Prell, D. Prendergast, C. D. Pemmaraju, D. M. Neumark, and S. R. Leone,

Structural Dynamics **4**, 044029 (2017).

[75] S. K. Cushing, M. Zürch, P. M. Kraus, L. M. Carneiro, A. Lee, H.-T. Chang, C. J. Kaplan, and S. R. Leone, Structural Dynamics **5**, 054302 (2018).

[76] M. F. Jager, C. Ott, P. M. Kraus, C. J. Kaplan, W. Pouse, R. E. Marvel, R. F. Haglund, D. M. Neumark, and S. R. Leone, Proceedings of the National Academy of Sciences **114**, 9558 (2017).

[77] J. Weisshaupt, A. Rouzée, M. Woerner, M. J. J. Vrakking, T. Elsaesser, E. L. Shirley, and A. Borgschulte, Phys. Rev. B **95**, 081101 (2017).

[78] L. M. Carneiro, S. K. Cushing, C. Liu, Y. Su, P. Yang, A. P. Alivisatos, and S. R. Leone, Nature Materials **16**, 819 (2017).

[79] A. Moulet, J. B. Bertrand, T. Klostermann, A. Guggenmos, N. Karpowicz, and E. Goulielmakis, Science **357**, 1134 (2017).

[80] Z. Schumacher, S. Sato, S. Neb, A. Niedermayr, L. Gallmann, A. Rubio, and U. Keller, Proceedings of the National Academy of Sciences **120** (2023), 10.1073/pnas.2221725120.

[81] M. Volkov, S. A. Sato, F. Schlaepfer, L. Kasmi, N. Hartmann, M. Lucchini, L. Gallmann, A. Rubio, and U. Keller, Nature Physics **15**, 1145 (2019).

[82] A. Niedermayr, M. Volkov, S. Sato, N. Hartmann, Z. Schumacher, S. Neb, A. Rubio, L. Gallmann, and U. Keller, Physical Review X **12**, 021045 (2022).

[83] C. J. Kaplan, P. M. Kraus, A. D. Ross, M. Zürch, S. K. Cushing, M. F. Jager, H.-T. Chang, E. M. Gullikson, D. M. Neumark, and S. R. Leone, Physical Review B **97**, 205202 (2018).

[84] C. J. Kaplan, P. M. Kraus, E. M. Gullikson, L. J. Borja, S. K. Cushing, M. Zürch, H.-T. Chang, D. M. Neumark, and S. R. Leone, Journal of the Optical Society of America B **36**, 1716 (2019).

[85] R. Géneaux, C. J. Kaplan, L. Yue, A. D. Ross, J. E. Bækhøj, P. M. Kraus, H.-t. Chang, A. Guggenmos, M.-y. Huang, M. Zürch, K. J. Schafer, D. M. Neumark, M. B. Gaarde, and S. R. Leone, Physical Review Letters **124**, 207401 (2020).

[86] D. M. Roessler, British Journal of Applied Physics **16**, 1359 (1965).

[87] M. Lucchini, S. A. Sato, G. D. Lucarelli, B. Moio, G. Inzani, R. Borrego-Varillas, F. Frassetto, L. Poletto, H. Hübener, U. De Giovannini, A. Rubio, and M. Nisoli, Nature Communications **12**, 1021 (2021).

[88] A. Mysyrowicz, D. Hulin, A. Antonetti, A. Migus, W. T. Masselink, and H. Morkoç, Physical Review Letters **56**, 2748 (1986).

[89] G. D. Mahan, Physical Review B **15**, 4587 (1977).

[90] G. L. Dolso, B. Moio, G. Inzani, N. D. Palo, S. A. Sato, R. Borrego-Varillas, M. Nisoli, and M. Lucchini, Opt. Express **30**, 12248 (2022).

[91] G. D. Lucarelli, B. Moio, G. Inzani, N. Fabris, L. Moscardi, F. Frassetto, L. Poletto, M. Nisoli, and M. Lucchini, Review of Scientific Instruments **91**, 053002 (2020).

[92] M. Lucchini, S. A. Sato, A. Ludwig, J. Herrmann, M. Volkov, L. Kasmi, Y. Shinohara, K. Yabana, L. Gallmann, and U. Keller, Science **353**, 916 (2016).

[93] M. Lucchini, S. A. Sato, F. Schlaepfer, K. Yabana, L. Gallmann, A. Rubio, and U. Keller, Journal of Physics: Photonics **2**, 025001 (2020).

[94] M. Volkov, S. A. Sato, A. Niedermayr, A. Rubio, L. Gallmann, and U. Keller, Phys. Rev. B **107**, 184304 (2023).

[95] S. Y. Kruchinin, F. Krausz, and V. S. Yakovlev, Reviews of Modern Physics **90**, 21002 (2018).

[96] S. A. Sato, M. Lucchini, M. Volkov, F. Schlaepfer, L. Gallmann, U. Keller, and A. Rubio, Physical Review B **98**, 035202 (2018).

[97] S. A. Sato, Computational Materials Science **194**, 110274 (2021).

[98] G. Inzani, A. Eskandari-asl, L. Adamska, B. Moio, G. L. Dolso, N. D. Palo, L. J. D'Onofrio, A. Lamperti, A. Molle, C. A. Rozzi, R. Borrego-Varillas, M. Nisoli, S. Pittalis, A. Avella, and M. Lucchini, "Photoinduced charge carrier dynamics in germanium," (2023), Nuovo Cimento C, Accepted.

[99] A. P. Jauho and K. Johnsen, Physical Review Letters **76**, 4576 (1996).

[100] C. Heide, T. Boolakee, T. Higuchi, and P. Hommelhoff, Phys. Rev. A **104**, 023103 (2021).

[101] M. S. Wismer, S. Y. Kruchinin, M. Ciappina, M. I. Stockman, and V. S. Yakovlev, Physical Review Letters **116**, 197401 (2016).

[102] H. Mashiko, K. Oguri, T. Yamaguchi, A. Suda, and H. Gotoh, Nature Physics **12**, 741 (2016).

[103] H. Mashiko, Y. Chisuga, I. Katayama, K. Oguri, H. Masuda, J. Takeda, and H. Gotoh, Nature Communications **9**, 1468 (2018).

[104] M. Schultze, K. Ramasesha, C. D. Pemmaraju, S. A. Sato, D. Whitmore, A. Gandman, J. S. Prell, L. J. Borja, D. Prendergast, K. Yabana, D. M. Neumark, and S. R. Leone, Science **346**, 1348 (2014).

[105] F. Schlaepfer, M. Lucchini, S. A. Sato, M. Volkov, L. Kasmi, N. Hartmann, A. Rubio, L. Gallmann, and U. Keller, Nature Physics **14**, 560 (2018).

[106] B. Buades, A. Picón, E. Berger, I. León, N. Di Palo, S. L. Cousin, C. Cocchi, E. Pellegrin, J. H. Martin, S. Mañas-Valero, E. Coronado, T. Danz, C. Draxl, M. Uemoto, K. Yabana, M. Schultze, S. Wall, M. Zürch, and J. Biegert, Applied Physics Reviews **8**, 011408 (2021).

[107] C. Schmidt, J. Bühler, A.-C. Heinrich, J. Allerbeck, R. Podzimski, D. Berghoff, T. Meier, W. G. Schmidt, C. Reichl, W. Wegscheider, D. Brida, and A. Leitenstorfer, Nature Communications **9**, 2890 (2018).

[108] T. Tritschler, O. D. Mücke, and M. Wegener, Phys. Rev. A **68**, 033404 (2003).

[109] F. Krausz and M. I. Stockman, Nature Photonics **8**, 205 (2014).

[110] T. Otobe, Y. Shinohara, S. A. Sato, and K. Yabana, Phys. Rev. B **93**, 045124 (2016).

[111] A. Eskandari-asl and A. Avella, "Dynamical projective operatorial approach (dpoa) for out-of-equilibrium systems and its application to tr-arpes," (2023), arXiv:2307.01244 [cond-mat.mtrl-sci].

[112] "CXRO, The center for X-ray optics," https://henke.lbl.gov/optical_constants/, accessed: 2023-08-02.

[113] "X-Ray Data Booklet," https://xdb.lbl.gov/Section1/Table_1-1a.htm, accessed: 2023-08-02.

[114] B. Buades, D. Moonshiram, T. P. H. Sidiropoulos, I. León, P. Schmidt, I. Pi, N. Di Palo, S. L. Cousin, A. Picón, F. Koppens, and J. Biegert, Optica **5**, 502 (2018).

[115] A. M. Summers, S. Severino, M. Reduzzi, T. P. H. Sidiropoulos, D. E. Rivas, N. Di Palo, H.-W. Sun, Y.-H. Chien, I. León, B. Buades, S. L. Cousin, S. M. Teichmann, T. Mey, K. Mann, B. Keitel, E. Plönjes, D. K. Efetov, H. Schwoerer, and J. Biegert, Ultrafast Science **3**, 1 (2023).

[116] B. Feuerbacher, M. Skibowski, R. P. Godwin, and T. Sasaki, J. Opt. Soc. Am. **58**, 1434 (1968).

[117] A. Ashoka, R. R. Tamming, A. V. Girija, H. Bretscher, S. D. Verma, S.-D. Yang, C.-H. Lu, J. M. Hodgkiss, D. Ritchie, C. Chen, C. G. Smith, C. Schnedermann, M. B. Price, K. Chen, and A. Rao, Nature Communications **13**, 1437 (2022).

[118] V. Smejkal, C. Trovatello, Q. Li, S. D. Conte, A. Marini, X. Zhu, G. Cerullo, and F. Libisch, Optics Express **31**, 107 (2023).

[119] T. P. H. Sidiropoulos, N. Di Palo, D. E. Rivas, S. Severino, M. Reduzzi, B. Nandy, B. Bauerhenne, S. Krylow, T. Vasileiadis, T. Danz, P. Elliott, S. Sharma, K. Dewhurst, C. Ropers, Y. Joly, M. E. Garcia, M. Wolf, R. Ernstorfer, and J. Biegert, Physical Review X **11**, 041060 (2021).

[120] A. R. Attar, H.-T. Chang, A. Britz, X. Zhang, M.-F. Lin, A. Krishnamoorthy, T. Linker, D. Fritz, D. M. Neumark, R. K. Kalia, A. Nakano, P. Ajayan, P. Vashishta, U. Bergmann, and S. R. Leone, ACS Nano , 15829–15840 (2020).

[121] H.-T. Chang, A. Guggenmos, C. T. Chen, J. Oh, R. Géneaux, Y.-D. Chuang, A. M. Schwartzberg, S. Aloni, D. M. Neumark, and S. R. Leone, Phys. Rev. B **104**, 064309 (2021).

[122] J. Oh, H.-T. Chang, C. T. Chen, S. Aloni, A. Schwartzberg, and S. R. Leone, The Journal of Physical Chemistry C , 5004 (2023).

[123]M. Lucchini, L. Castiglioni, L. Kasmi, P. Kliuiev, A. Ludwig, M. Greif, J. Osterwalder, M. Hengsberger, L. Gallmann, and U. Keller, Physical Review Letters 115, 137401 (2015).

[124]A. Cirri, J. Husek, S. Biswas, and L. R. Baker, The Journal of Physical Chemistry C 121, 15861 (2017).

[125]B. L. Henke, E. M. Gullikson, and J. C. Davis, Atomic data and nuclear data tables 54, 181 (1993).

[126]M. Merano, Physical Review A 93, 013832 (2016).

[127]A. B. Kuzmenko, Review of Scientific Instruments 76, 083108 (2005).

[128]M. Volkov, J. Pupeikis, C. R. Phillips, F. Schlaepfer, L. Gallmann, and U. Keller, Optics Express 27, 7886 (2019).

[129]F. Lücking, A. Trabattoni, S. Anumula, G. Sansone, F. Calegari, M. Nisoli, T. Oksenhendler, and G. Tempea, Optics Letters 39, 2302 (2014).

[130]K. Kato, H. Mashiko, Y. Kunihashi, H. Omi, H. Gotoh, and K. Oguri, Optics Express 28, 1595 (2020).

[131]C. Schriever, S. Lochbrunner, E. Riedle, and D. J. Nesbitt, Review of Scientific Instruments 79, 013107 (2008).

[132]Y. Feng, I. Vinogradov, and N.-H. Ge, Optics Express 25, 26262 (2017).

[133]T. Heinrich, H.-T. Chang, S. Zayko, K. Rossnagel, M. Sivis, and C. Ropers, Physical Review X 13, 021033 (2023).

[134]V. Stooß, M. Hartmann, P. Birk, G. D. Borisova, T. Ding, A. Blättermann, C. Ott, and T. Pfeifer, Review of Scientific Instruments 90, 053108 (2019).

[135]T. Gutberlet, H.-T. Chang, S. Zayko, M. Sivis, and C. Ropers, Optics Express 31, 39757 (2023).

[136]J. J. Abel, F. Wiesner, J. Nathanael, J. Reinhard, M. Wünsche, G. Schmidl, A. Gawlik, U. Hübner, J. Plentz, C. Rödel, G. G. Paulus, and S. Fuchs, Optics Express 30, 35671 (2022).

[137]K. Yao, F. Willems, C. von Korff Schmising, C. Strüber, P. Hessing, B. Pfau, D. Schick, D. Engel, K. Gerlinger, M. Schneider, and S. Eisebitt, Review of Scientific Instruments 91, 093001 (2020).

[138]F. Willems, C. von Korff Schmising, C. Strüber, D. Schick, D. W. Engel, J. K. Dewhurst, P. Elliott, S. Sharma, and S. Eisebitt, Nature Communications 11, 871 (2020).

[139]R. Géneaux, H.-T. Chang, A. M. Schwartzberg, and H. J. B. Marroux, Optics Express 29, 951 (2021).

[140]D. Faccialà, B. W. Toulson, and O. Gessner, Optics Express 29, 35135 (2021).

[141]J. S. Toll, Physical Review 104, 1760 (1956).

[142]D. M. Roessler, British Journal of Applied Physics 16, 1119 (1965).

[143]V. Leshchenko, S. J. Hageman, C. Cariker, G. Smith, A. Camper, B. K. Talbert, P. Agostini, L. Argenti, and L. F. DiMauro, Optica 10, 142 (2023).

[144]S. Bengtsson, E. W. Larsen, D. Kroon, S. Camp, M. Miranda, C. L. Arnold, A. L'Huillier, K. J. Schafer, M. B. Gaarde, L. Rippe, and J. Mauritsson, Nature Photonics 11, 252 (2017).

[145]K. H. Stone, S. M. Valvidares, and J. B. Kortright, Physical Review B 86, 024102 (2012).

[146]A. Camper, H. Park, S. J. Hageman, G. Smith, T. Auguste, P. Agostini, and L. F. DiMauro, Optics Letters 44, 5465 (2019).

[147]X. Zhou, R. Lock, W. Li, N. Wagner, M. M. Murnane, and H. C. Kapteyn, Physical Review Letters 100, 073902 (2008).

[148]R. M. Lock, X. Zhou, W. Li, M. M. Murnane, and H. C. Kapteyn, Chemical Physics 366, 22 (2009).

[149]O. Smirnova, Y. Mairesse, S. Patchkovskii, N. Dudovich, D. Villeneuve, P. Corkum, and M. Y. Ivanov, Nature 460, 972 (2009).

[150]J. B. Bertrand, H. J. Wörner, P. Salières, D. M. Villeneuve, and P. B. Corkum, Nature Physics 9, 174 (2013).

[151]A. Camper, T. Ruchon, D. Gauthier, O. Gobert, P. Salières, B. Carré, and T. Auguste, Physical Review A 89, 043843 (2014).

[152]A. Camper, E. Skantzakis, R. Géneaux, F. Risoud, E. English, Z. Diveki, N. Lin, V. Gruson, T. Auguste, B. Carré, R. R. Lucchese, A. Maquet, R. Taïeb, J. Caillat, T. Ruchon, and P. Salières, Optica 8, 308 (2021).

[153]A. Camper, A. Ferré, V. Blanchet, F. Burgy, D. Descamps, S. Petit, T. Ruchon, and Y. Mairesse, Optics Letters 40, 5387 (2015).

[154]A. Sommer, E. M. Bothschafter, S. A. Sato, C. Jakubeit, T. Latka, O. Razskazovskaya, H. Fattahi, M. Jobst, W. Schweinberger, V. Shirvanyan, V. S. Yakovlev, R. Kienberger, K. Yabana, N. Karpowicz, M. Schultze, and F. Krausz, Nature 534, 86 (2016).

[155]F. Krausz, Physica Scripta 91, 063011 (2016).

[156]F. Calegari, G. Sansone, S. Stagira, C. Vozzi, and M. Nisoli, Journal of Physics B: Atomic, Molecular and Optical Physics 49, 062001 (2016).

[157]K. Midorikawa, Nature Photonics 16, 267 (2022).

[158]P. B. Corkum, Physical Review Letters 71, 1994 (1993).

[159]K. Kulander, K. Schafer, and J. Krause, NATO Advanced Science Institutes Series 316, 95 (1993).

[160]K. Schafer, B. Yang, L. DiMauro, and K. Kulander, Physical review letters 70, 1599 (1993).

[161]X. Ren, J. Li, Y. Yin, K. Zhao, A. Chew, Y. Wang, S. Hu, Y. Cheng, E. Cunningham, Y. Wu, M. Chini, and Z. Chang, Journal of Optics 20, 023001 (2018).

[162]J. Li, X. Ren, Y. Yin, K. Zhao, A. Chew, Y. Cheng, E. Cunningham, Y. Wang, S. Hu, Y. Wu, M. Chini, and Z. Chang, Nature Communications 8, 186 (2017).

[163]G. Sansone, E. Benedetti, F. Calegari, C. Vozzi, L. Avaldi, R. Flammini, L. Poletto, P. Villoresi, C. Altucci, R. Velotta, S. Stagira, S. De Silvestri, and M. Nisoli, Science 314, 443 (2006).

[164]M. Chini, S. Gilbertson, S. D. Khan, and Z. Chang, Optics Express 18, 13006 (2010).

[165]T. Gaumnitz, A. Jain, Y. Pertot, M. Huppert, I. Jordan, F. Ardana-Lamas, and H. J. Wörner, Optics Express 25, 27506 (2017).

[166]S. L. Cousin, N. Di Palo, B. Buades, S. M. Teichmann, M. Reduzzi, M. Devetta, A. Kheifets, G. Sansone, and J. Biegert, Physical Review X 7, 041030 (2017).

[167]A. S. Johnson, D. R. Austin, D. A. Wood, C. Brahms, A. Gregory, K. B. Holzner, S. Jarosch, E. W. Larsen, S. Parker, C. S. Strüber, P. Ye, J. W. G. Tisch, and J. P. Marangos, Science Advances 4 (2018).

[168]B. Major, K. Kovács, E. Svirplys, M. Anus, O. Ghafur, K. Varjú, M. J. J. Vrakking, V. Tosa, and B. Schütte, Phys. Rev. A 107, 023514 (2023).

[169]Y. Yang, R. E. Mainz, G. M. Rossi, F. Scheiba, M. A. Silva-Toledo, P. D. Keathley, G. Cirmi, and F. X. Kärtner, Nature Communications 12, 6641 (2021).

[170]S. M. Teichmann, F. Silva, S. L. Cousin, M. Hemmer, and J. Biegert, Nature Communications 7, 11493 (2016).

[171]T. P. H. Sidiropoulos, N. D. Palo, D. E. Rivas, A. Summers, S. Severino, M. Reduzzi, and J. Biegert, Nature Communications 14, 7407 (2023).

[172]F. J. Furch, T. Witting, M. Osolodkov, F. Schell, C. P. Schulz, and M. J. J Vrakking, Journal of Physics: Photonics 4, 032001 (2022).

[173]T. Okamoto, Y. Kunihashi, Y. Shinohara, H. Sanada, M.-C. Chen, and K. Oguri, Optics Letters 48, 2579 (2023).

[174]S. Hädrich, Jan Rothhardt, M. Krebs, S. Demmler, A. Klenke, A. Tünnermann, and J. Limpert, Journal of Physics B: Atomic, Molecular and Optical Physics 49, 172002 (2016).

[175]D. Garratt, L. Misiekis, D. Wood, E. W. Larsen, M. Matthews, O. Alexander, P. Ye, S. Jarosch, C. Ferchaud, C. Strüber, et al., Nature Communications 13, 3414 (2022).

[176]C. N. R. Rao, Annual Review of Physical Chemistry 40, 291 (1989).